

X-ray spectral variability of seven LINER nuclei with *XMM-Newton* and *Chandra* data

Hernández-García, L.¹; González-Martín, O.^{2,3}; Márquez, I.¹; Masegosa, J.¹

¹ Instituto de Astrofísica de Andalucía, CSIC, Glorieta de la Astronomía, s/n, 18008 Granada, Spain

e-mail: lorena@iaa.es

² Instituto de Astrofísica de Canarias (IAC), C/Vía Lactea, s/n, 38205 La Laguna, Tenerife, Spain

³ Departamento de Astrofísica, Universidad de La Laguna (ULL), 38205 La Laguna, Tenerife, Spain

Received XXXX/ accepted YYYY

ABSTRACT

Context. One of the most important features in active galactic nuclei (AGN) is the variability of their emission. Variability has been discovered at X-ray, UV, and radio frequencies on time scales from hours to years. Among the AGN family and according to theoretical studies, Low-Ionization Nuclear Emission Line Region (LINER) nuclei would be variable objects on long time scales.

Aims. Our purpose is to investigate spectral X-ray variability in LINERs and to understand the nature of these kinds of objects, as well as their accretion mechanism.

Methods. *Chandra* and *XMM-Newton* public archives were used to compile X-ray spectra of seven LINER nuclei at different epochs with time scales of years. To search for variability we fit all the spectra from the same object with a set of models, in order to identify the parameters responsible for the variability pattern. We also analyzed the light curves in order to search for short time scale (from hours to days) variability. Whenever possible, UV variability was also studied.

Results. We found spectral variability in four objects (namely NGC 1052, NGC 3226, NGC 4278, and NGC 4552), with variations mostly related to hard energies (2-10 keV). These variations are due to changes in the soft excess, and/or changes in the absorber, and/or intrinsic variations of the source. These variations were within years, the shorter time scale being found for NGC 4278 (two months). Another two galaxies (NGC 4261 and NGC 5846) seem not to vary. Short time scale variations during individual observations were not found. Our analysis confirms the previously reported anticorrelation between the X-ray spectral index, Γ , and the Eddington ratio, $L_{\text{bol}}/L_{\text{Edd}}$, and also the correlation between the X-ray to UV flux ratio, α_{ox} , and the Eddington ratio, $L_{\text{bol}}/L_{\text{Edd}}$. These results support an Advection Dominated Accretion Flow (ADAF) as the accretion mechanism in LINERs.

Conclusions.

Key words. Galaxies: active – galaxies: individual X-rays: galaxies – Ultraviolet: galaxies – Accretion

1. Introduction

The plethora of phenomena present in an active galactic nucleus (AGN) shows the existence of energetic processes in the nuclei of galaxies that cannot be attributed to stars (Peterson 1997). The unified model for AGN (Urry & Padovani 1995; Antonucci 1993) represents a scenario where the central, supermassive black hole (SMBH) is surrounded by a dusty torus; and depending on the line of sight of the observer, the AGN appears as type 1 (pole-on view) or type 2 (edge on view). However, even if, broadly speaking, the unified model is a good representation of AGN, there are a number of objects that still cannot be fitted under this scheme. This is the case of Low Ionisation Nuclear Emission Line Regions (LINERs), which are the main purpose of this research.

First defined by Heckman (1980), the characterization of LINERs was made in the optical, where their spectra show strong low-ionization lines such as [OI] λ 6300Å and [SII] λ 6717, 6731Å (Veilleux & Osterbrock 1987). Different options have been proposed to explain the ionization mechanism in LINERs, such as shock-heated gas (Dopita & Sutherland 1995), photoionization by hot stars (Terlevich & Melnick 1985), by post main sequence stars (Cid-Fernandes et al 2011), or a low luminosity active galactic nuclei (Ho et al. 1993). Today, the

most accepted option is that they harbour AGN (see Ho 2008; Márquez 2012).

X-ray data for LLAGN offer the most reliable probe of the high-energy spectrum, providing many AGN signatures (D’Onofrio et al. 2012). In LINERs it can be assessed that an AGN is present when a point-like source is detected at hard X-ray energies (Satyapal et al. 2004, 2005; Dudik et al. 2005; Ho 2008). The most extensive work has been carried out by González-Martín et al. (2009b), who analyzed 82 LINERs with *Chandra* and/or *XMM-Newton* data for single period observations. They found that 60% of the sample showed a compact nuclear source in the 4.5-8 keV band; a multiwavelength analysis resulted in about 80% of the sample showing evidence of AGN-related properties, which is a lower limit since Compton-thick objects were not taken into account.

It is tempting to view LINERs as a scaled-down version of Seyfert galaxies, but in fact they are qualitatively different from their neighbouring class (Ho 2008). LINERs have lower luminosities ($L_{2-10\text{keV}} \approx 10^{39} - 10^{42} \text{ erg s}^{-1}$), lower Eddington ratios ($L_{\text{bol}}/L_{\text{Edd}} \approx 10^{-4}$) and more massive black holes ($M_{\text{BH}} \approx 10^8 M_{\odot}$) (Eracleous et al. 2010a; Masegosa et al. 2011).

Variability is one of the main properties that characterizes AGN, most of these being at least mildly variable. When quasars were first discovered in the 1960s (Schmidt 1963), one of their

key defining properties was their variability. These objects are variable over the entire wavelength range, many of them varying 0.3-0.5 magnitudes over time scales of a few months, and others varying significantly on time scales as short as a few days (Peterson 1997). Variability properties seem to correlate with AGN power; in quasars, variations likely result from both accretion disk instability and microlensing, while in Seyfert galaxies the brightness of the nucleus is thought to vary, the broad-line region (BLR) responding to these changes a few weeks later (D’Onofrio et al. 2012).

At X-ray frequencies many studies have been made to understand variability in Seyfert galaxies. Risaliti et al. (2000) studied the highly variable Seyfert 1.8 galaxy NGC 1365, which was observed for many years with different instruments; they also found variability in the Seyfert galaxy UGC 4203 using *Chandra* data (Risaliti et al. 2010). They suggested a scenario in which the variability is produced by clouds intersecting the line of sight to the observer. Evans et al. (2005) found that the 2-10 keV luminosity for NGC 6251 varied a factor of ≈ 5 from 1991 to 2003. More recently, a study made by Caballero-Garcia et al. (2012) showed that the five Seyfert galaxies studied with *Swift*/BAT showed flux variability on time-scales of 1-2 days. Narrow-Line Seyfert 1 galaxies (NLSy1) also show variability in X-rays (Panessa et al. 2011; Risaliti et al. 2011).

As stated by Ptak et al. (1998), “LINERs tend to show little or no significant short-term variability (i.e., with timescales less than a day)” (see also Krolik 1999). The first clear evidence of variability in LINERs was reported by Maoz et al. (2005) at UV frequencies, where all but three objects in their sample of 17 type 1 and 2 LINERs appeared variable. The works by Pian et al. (2010) and Younes et al. (2011) at X-ray energies for type 1 LINERs agrees with the consideration of variability being a common property of LINERs. González-Martín et al. (2011a) studied a *Suzaku* observation of 80 ks of the *Compton*-thick LINER NGC 4102, who found two absorbers from the soft X-rays and the optical spectrum. They found variations of the soft-excess flux within ≈ 7 years comparing with *Chandra* data. This variation was described by a decrease in the normalisation of the power-law component and the thermal component by a factor of ≈ 7 . Thus it is important to characterize the phenomenon fully, both the scale and magnitude of the variability. Taking the predictions by McHardy et al. (2006) of the time-scale variations scaling with black hole masses, M_{BH} , and bolometric luminosities, L_{bol} , González-Martín & Vaughan (2012) estimate time scales larger than tens of days in LINERs.

This paper is organized as follows: in Section 2 we present the sample and the data. The reduction of the data is explained in Section 3. Our methodology is described in Section 4, where individual and simultaneous spectral fittings, comparisons when different apertures were used, flux variability in X-rays and UV frequencies, and short term variability subsections are explained. The results from this analysis are given in Section 5, and a discussion in Section 6. Finally our main results are summarized in Section 7.

2. The sample and the data

From the sample of 82 type 1 and 2 LINERs of González-Martín et al. (2009b) we searched in the current literature for hints of variability by means of differences in luminosity when different observations are considered. We used the HEASARC¹ archive to search for different observations

with *Chandra* and *XMM-Newton*, with public available data until October 2012. This analysis provided us with 16 candidate variable sources. The four ULIRGs in this primary selection (NGC 3690, NGC 6240, IRAS 17208-0014, and UGC 08696) were discarded since our aim is to deal with typical pure LINERs (see Ho 2008), not contaminated by strong star formation where other ionization sources could be at work. NGC 4636 was also discarded because its X-ray emission is dominated by the cluster emission. We also rejected from the present analysis all the observations affected by pile-up larger than 10% (*Chandra* data observations for objects namely NGC 4579, NGC 3998, NGC 4594, and NGC 6251 and three *Chandra* observations of NGC 4278). Finally, to guarantee a proper spectral fitting we kept only observations with a minimum of 400 number counts. An exception was made with obsID 11269 for NGC 4278, which met this criterion, but visual inspection revealed a very low count number in the hard band.

The final sample of LINERs contains seven objects. Table 1 shows the general properties of the target galaxies for this study and Table 2 the log of the observations. Number of counts and hardness ratios, defined as $HR = (H-S)/(H+S)$, where H is the number of counts in the hard (2-10 keV) band and S is the number of counts in the soft (0.5-2 keV) band, are also presented. For five sources, NGC 1052, NGC 3226, NGC 4261, NGC 4278, and NGC 5846, observations at different epochs were taken with the same instrument, providing us with good examples for variability studies. In the other two sources, NGC 3627, and NGC 4552, we can estimate variability only by comparing *XMM-Newton* with *Chandra* data. These results should be viewed with caution due to the different apertures used by both instruments. A detailed study of the extended emission is made in these two objects (see Section 4).

3. Data reduction

Data reduction was performed following the procedure described by González-Martín et al. (2009b). We review the methodology here.

3.1. *Chandra* data

Chandra observations were obtained with the ACIS instrument (Garmire et al. 2003). The data reduction and analysis were carried out in a systematic, uniform way using CXC Chandra Interactive Analysis of Observations (CIAO²), version 4.3. Level 2 event data were extracted by using the task `ACIS-PROCESS-EVENTS`. We first cleaned the data from background flares (i.e. periods of high background) that could affect our analysis. These “flares” are due to low energy photons that interact with the detector. To clean them we use the task `LC_CLEAN.SL`³, that removes periods of anomalously low (or high) count rates from lightcurves, from source-free background regions of the CCD. This routine calculates a mean rate from which it deduces a minimum and maximum valid count rate, and creates a file with those periods which are considered by the algorithm to be good.

Nuclear spectra were extracted from a circular region centered at the positions given by NED⁴. We chose circular radii, trying to get all the possible photons, but not including other sources or background effects. The radii are in the range between 3-8” (or 6-16 pixels, see Tab. 2). The background se-

² <http://cxc.harvard.edu/ciao4.4/>

³ http://cxc.harvard.edu/ciao/ahelp/lc_clean.html

⁴ <http://ned.ipac.caltech.edu/>

¹ <http://heasarc.gsfc.nasa.gov/>

lection was made taking regions free of sources, in the same chip as the target, and close to the source (5'' for NGC 3627, NGC 4278, NGC 4261, and NGC 4552 and 7'' for NGC 5846 and NGC 3627), to minimize effects related to the spatial variations of the CCD response.

We used the DMEXTRACT task to extract the spectra of the source and the background regions. The response matrix file (RMF) and ancillary reference file (ARF) were generated for each source region using the MKACISRMF and MKWARF tasks, respectively. Before the background subtraction, the spectra were binned to have a minimum of 20 counts per spectral bin, to be able to use the χ^2 -statistics. This was done by using the GRPPHA task included in FTOOLS.

3.2. XMM-Newton data

All of the XMM-Newton observations were obtained from the EPIC pn camera⁵. The data were reduced in a systematic, uniform way using the Science Analysis Software (SAS⁶), version 11.0.0. Before the extraction of the spectra, good-timing periods were selected (i.e. “flares” were excluded). The method used for this purpose maximizes the S/N ratio of the net source spectrum by applying a different constant count rate threshold on the single-events, $E > 10$ keV field-of-view background light curve. The nuclear positions were taken from NED, while the extraction region was determined through circles of 25'' radius and the background was determined by using an algorithm that selects the best circular region around the source, free of other sources and as close as possible to the nucleus. This automatic selection was checked manually to ensure the best selection for the backgrounds.

The extraction of the source and the background regions were done by using the EVSELECT task. Response matrix files (RMF) were generated using the RMFGEN task, and the ancillary response files (ARF) were generated using the ARFGEN task. We then grouped the spectra to get at least 20 counts per spectral bin using the GRPPHA task, as is required to use the χ^2 -statistics.

3.3. Light curves

Light curves in the 0.5-10 keV band for the source and background were extracted using the DMEXTRACT task for XMM-Newton and EVSELECT task for Chandra with a 1000 s bin. The light curve from the source was manually screened for high background and flaring activity. This means that when the background light curve showed flare-like events and/or prominent decreasing/increasing trends, we did not use those intervals. After rejection of the respective time intervals, the total useful time for each observation was usually less than the original exposure time (see Table 2). The light curves are shown in Figs. C.1-C.7, where the solid line represents the mean value of the count-rate and the dashed lines represent 1σ standard deviation.

4. Methodology

The spectral fitting process comprises two steps: (1) individual analysis of each observation to determine the best fit for each spectrum, and (2) simultaneous fitting of the set of spectra of the

same object at different epochs. The spectral fitting was done using XSPEC⁷ version 12.7.0.

4.1. Individual spectral analysis

We have performed an individual study of the best fit model for each observation. For this, we follow the method used by González-Martín et al. (2009b), where five different models were used:

1. ME: A pure thermal model (MEKAL in XSPEC). The thermal emission is responsible for the bulk of the X-ray energy distribution. The free parameters in this model are the column density, N_H , the temperature, kT , and the normalization, $Norm$.
2. PL: A single power law model, which corresponds to a non-thermal source representing an AGN. The column density, N_H , is added as a free parameter, to take the absorption by matter along our line of sight to the target into account. The free parameters in this model are the column density, N_H , the slope of the power law, Γ , and the normalization, $Norm$.
3. 2PL: A model containing two power laws with the same slope, Γ . Here the bulk of the hard X-rays is due to a primary continuum described by a power law, and the soft X-rays come from a scattering component described by the other power law. The free parameters in this model are the column densities, N_{H1} and N_{H2} , the slope of the power-law, Γ , and the normalizations, $Norm_1$ and $Norm_2$.
4. MEPL: A composite of a thermal plus a single power law model. The AGN dominates the hard X-rays, but the soft X-rays require an additional thermal contribution. The free parameters in this model are the column densities, N_{H1} and N_{H2} , the temperature, kT , the slope of the power law, Γ , and the normalizations, $Norm_1$ and $Norm_2$.
5. ME2PL: A composite of a thermal plus two power laws model. This model is like MEPL but including the contribution of the thermal emission at soft X-rays. This is the *Compton-thin Seyfert 2 baseline* model used by Guainazzi et al. (2005). The free parameters in this model are the column densities, N_{H1} and N_{H2} , the temperature, kT , the slope of the power law, Γ , and the normalizations, $Norm_1$ and $Norm_2$.

For models 2PL, MEPL, and ME2PL we used two absorbers, N_{H1} and N_{H2} . These absorbers are included in the models as $abs(N_{H1}) * PL + abs(N_{H2}) * PL$, $abs(N_{H1}) * Mekeal + abs(N_{H2}) * PL$, and $abs(N_{H1}) * (PL) + Mekeal + abs(N_{H2}) * PL$. The Galactic absorption was included in each model and was fixed to the predicted value (Col. 7 in Table 1) using the NH tool within FTOOLS (Dickey & Lockman 1990; Kalberla et al. 2005). We searched for the presence of the neutral iron fluorescence emission line, $FeK\alpha$, adding a narrow Gaussian with centroid energy fixed at the observed energy corresponding to a rest frame at 6.4 keV. Two Gaussians were also included to model recombination lines, $FeXXV$ at 6.7 keV and $FeXXVI$ at 6.95 keV.

We impose the following conditions to the resulting best-fit parameters to ensure a physical meaning to the best-fit solutions: $\Gamma > 0.5$, $N_{H1} > N_{Gal}$ and $N_{H2} > N_{H1}$.

We select as the best fit the spectral fitting with $\chi^2/d.o.f$ closer to unity and the F-test probability less than 10^{-5} when comparing with a simpler model (Box 1953). Thus, the best fit model is the simplest model which represents the data.

⁵ EPIC pn is the most efficient camera because X-ray photons hit the detector from the rear side, avoiding cross-calibration problems between the pn and MOS cameras (Strüder et al. 2001)

⁶ <http://xmm.esa.int/sas/>

⁷ <http://heasarc.gsfc.nasa.gov/xanadu/xspec/>

4.2. Simultaneous spectral analysis

The aim of this analysis is to detect variability and study the physical parameters governing its pattern for these sources. For that we simultaneously fitted the spectra for each object to the same model. The baseline model for this simultaneous fit was the best fit obtained for the individual fitting of the observations. When the best fit for individual sources did not match for all the observations, we used the most complex one. For each galaxy, the initial values for the parameters were set to those obtained for the spectrum with the largest number of counts.

The simultaneous fit was made in three steps. First, every spectrum was fitted with the same model and all the parameters linked to the same value (hereinafter SMF0). If this model was able to fit all the spectra, then the source is not variable. SMF0 was used as the baseline model for the next step otherwise. Secondly, we let the parameters: N_{H1} , N_{H2} , Γ , $Norm1$, $Norm2$, and kT vary individually (hereinafter SMF1). Among these we chose the best fit as that with $\chi_r^2 = \chi^2/d.o.f$ closest to the unity and that improved the SMF0 fit (using the F-test). The result of SMF1 was used as the baseline model for the next step. Finally, we also included the possibility that two parameters could vary together to explain the variability pattern of the sources. For that purpose we fitted each set of data, letting the parameter found as the best fit in SMF1 vary together with any of the other parameters of the fit (hereinafter SMF2). Again the χ_r^2 and F-test were used to determine whether this further complexity of the spectral fitting results in a significant improvement of the final fit.

The final best fit could be (1) SMF0: the best simultaneous fit with each parameters tied together for all the observations (i.e. non variable source); (2) SMF1: in the best simultaneous fit only one parameter was allowed to vary among the observations, and (3) SMF2: the best simultaneous fit was that with two parameters allowed to vary during the observations.

Further complexity of the spectral fitting (e.g. three parameters allowed to vary) were not required for our set of data (see Section 5).

4.2.1. Different apertures

When data from *Chandra* and *XMM-Newton* were used together, an additional analysis was performed to ensure that the extra-nuclear emission is not producing the observed variability.

Firstly, we extracted a spectrum from *Chandra* data with an aperture radius of $25''$. Secondly, a spectrum of an annular region was extracted from *Chandra* data, with $R_{ext} = 25''$ and $R_{int} = R_{Chandra}$ (Col. 4 in Table 2). When the contamination by the annular region to the $25''$ *Chandra* data emission was higher than 50% in the 0.5-10.0 keV energy band (see Section 5), we did not consider the joint analysis since the accuracy of the derived parameters could be seriously affected. For lower contamination levels, we considered that *Chandra* data could be used to estimate the contribution of the annular region to the *XMM-Newton* spectrum. We extracted the *Chandra* spectrum in that ring (from R_{int} to R_{ext}) and fitted the five models explained in Section 4.1. Then we included the resulting model, with its corresponding parameters frozen, in the fit of the *XMM-Newton* nuclear spectrum (the circular region with R_{ext}), and extracted the parameters for the nuclear emission. Appendix B.1 shows the images corresponding to the data used for this analysis, where the different apertures are shown. This analysis was made for all the seven objects with *Chandra* and *XMM-Newton* spectra taken in similar dates.

4.3. Flux variability

We computed X-ray luminosities for the individual and simultaneous fits. UV luminosities were also obtained when possible (see below).

4.3.1. X-ray luminosities

We computed the X-ray luminosities and sigma errors for the soft and hard bands using XSPEC. Note that distances of the sources were taken from NED. We assumed a given object as variable if the luminosity variation was larger than 3σ and as non-variable when its variations were below 1σ .

4.3.2. UV luminosities

Simultaneous *XMM-Newton* Optical Monitor (OM)⁸ data were used to compute the UV luminosities. This monitor has three different filters in the UV range, UVW2 centred at 1894\AA ($1805\text{-}2454$) \AA , UVM2 centred at 2205\AA ($1970\text{-}2675$) \AA , and UVW1 at 2675\AA ($2410\text{-}3565$) \AA . We used these three filters whenever possible.

We used the OM observation FITS source lists⁹ to get the photometry. We checked that the photometry using IRAF and the Vega magnitude system and calculating the luminosities by using SAS to estimate the count rate gave similar results. When OM data were not available we searched for UV information in the literature (see Appendix A).

When simultaneous observations from X-rays and UV with *XMM-Newton* were available, we computed the X-ray to UV flux ratio defined as:

$$\alpha_{ox} = \frac{\log(L_x/L_{UV})}{\log(v_x/v_{UV})} \quad (1)$$

where L_{UV} were computed from UVM2 and UVW1 filters and L_x was computed using the integral:

$$F_x(0.5 - 2.0\text{keV}) = \int_{0.5\text{keV}}^{2.0\text{keV}} F_v(2\text{keV}) \left(\frac{v}{v_{2\text{keV}}}\right)^{(1-\Gamma)} dv \quad (2)$$

leading to:

$$L(2\text{keV}) = \frac{L(0.5 - 2.0\text{keV})}{v_{2\text{keV}}} \frac{2 - \Gamma}{1 - 0.25^{2-\Gamma}} \quad (3)$$

4.4. Short time scale variability

We analyzed the light curves for each observation to check for variability on short time scales in the sample.

Assuming a constant count rate for the whole observation, we calculated the $\chi^2/d.o.f$ test as a first approximation to the variations. We considered the source to be variable if the count rate differed from the average above 3σ (or 99.7% probability).

To check the variability amplitude of the light curves, we calculated the normalized excess variance, σ_{NXS}^2 . We followed prescriptions given by Vaughan et al. (2003) to estimate σ_{NXS}^2 and its error, $\text{err}(\sigma_{NXS}^2)$ (see also González-Martín et al. (2011b)):

$$\sigma_{NXS}^2 = \frac{S^2 - \langle \sigma_{err}^2 \rangle}{\langle x \rangle^2} \quad (4)$$

⁸ http://xmm.esac.esa.int/external/xmm_user_support/documentation/technical/OM/

⁹ <ftp://xmm2.esac.esa.int/pub/odf/data/docs/XMM-SOC-GEN-ICD-0024.pdf>

$$\text{err}(\sigma_{NXS}^2) = \sqrt{\frac{2}{N} \left(\frac{\langle \sigma_{err}^2 \rangle}{\langle x \rangle^2} \right)^2 + \frac{\langle \sigma_{err}^2 \rangle}{N} \frac{4\sigma_{NXS}^2}{\langle x \rangle^2}} \quad (5)$$

where x , σ_{err} and N are the count rate, its error and the number of points in the light curve, respectively, and S^2 is the variance of the light curve:

$$S^2 = \frac{1}{N-1} \sum_{i=1}^N (x_i - \langle x \rangle)^2 \quad (6)$$

5. Results

5.1. Individual objects

Here we present the results of the variability of the seven sources individually. General results are given in Section 5.2. Each subsection describes the following: the observations used in the analysis (Table 2), variations of the hardness ratio (from Col. 8 in Table 2), individual and simultaneous best fit and the parameters varying in the model (see Tables 3, 4, 5 and Figure 1), X-ray flux variations (see Table 6 and Figure 2), the analysis of the annular region when data of *Chandra* and *XMM-Newton* were used together (Table 7 and Appendix B.1), and the simultaneous fittings of these observations (Table 8), short term variability from the analysis of the light curves (see Table 9 and Appendix C.1-C.7), and UV luminosities when simultaneous data from the OM monitor was available (Table 10, Figure 2). Moreover, a summary of the variability is given in Table 11. Notes and comparisons with previous works for individual objects are included in Appendix A.

5.1.1. NGC 1052

We used one *Chandra* and four *XMM-Newton* observations. These four *XMM-Newton* observations were taken from August 2001 to August 2009, and the *Chandra* observation was taken in August 2000 (see Table 2).

Variations of 33% (10%) in HR were obtained between the first and the last *XMM-Newton* (*Chandra*) observations (see Column 8 in Table 2).

The individual fits gave ME2PL as the best fit. In this case SMF2 was used, being the best representation of the observed differences (see Fig. 1) when varying $Norm_2$ and N_{H2} (see Tables 3, 4 and 5). Variations were 49% ($Norm_2$) and 31% (N_{H2}) between the first and the last observations.

In Fig. 2, variations of the soft and hard intrinsic luminosities of the simultaneous fitting are presented. At soft energies we found variations at 8.3σ (20%), and at hard energies at 7.5σ (20%), in a period of 8 years. The largest variation for $Norm_2$ was found between the second and the third observations (see Table 5), with an interval of 3 years, where both soft and hard luminosities varied 12% and 29% respectively (see Table 6). The strongest variation for N_{H2} was obtained between the first and the second observations (see Table 5), with a 32% change in 4 years.

We compared the *Chandra* observation from 2000 with the *XMM-Newton* observation from 2001 (see Figure B.1), following the prescriptions given in Sect. 4.2.1. The spectral analysis of *Chandra* data was included in Tables 5 and 6, which gave ME2PL as the best fit. The annular region represented a 10% of the 25'' *Chandra* aperture luminosity in the 0.5-10 keV band. The *Chandra* data for the 25'' radius circular region provided intrinsic luminosities representing 22% (75%) for the soft (hard)

energy of the emission from *XMM-Newton* data (see Table 6). After taking into account the contribution from the annular region, the analysis indicated no changes in one year period (see Tables 7 and 8) in the nuclear emission.

According to the values of χ_r^2 and σ^2 showed in Table 9, the analysis from the light curves did not show short time scale variations (see Figure C.1), neither *XMM-Newton* nor in *Chandra* data, since variations were below 3σ .

In Fig. 2 UV luminosities (Table 10) are represented for the UVW2 and UVM2 filters. Variations at 7.3σ (or 16-25 %) and 2σ (or 2-23%) were obtained, respectively.

5.1.2. NGC 3226

We used two *XMM-Newton* observations in November 2000 and December 2006 and one *Chandra* observation from December 1999.

Variations in the HR of 100% were obtained both in *Chandra* and in *XMM-Newton* data (see Column 8 in Table 2). However, ObsID 0400270101 from *XMM-Newton* was not used for further discussion (see below).

The observation from 2000 gave as best fit the 2PL model, while that from 2006 was best fitted with a PL. The simultaneous spectral fitting was better represented by a 2PL model varying N_{H2} (i.e. SMF1, Figure 1), with a 74% amplitude variation. The resulting parameters (see Tables 5 and 6) indicate that X-ray soft and hard intrinsic luminosity variations were below 1σ over a period of 6 years.

We compared the *Chandra* observation from 1999 with the *XMM-Newton* observation from 2000. The spectral analysis of *Chandra* data was included in Tables 5 and 6. The contribution from the annular region to the 25'' aperture *Chandra* data was 20% in the 0.5-10.0 keV band. The *Chandra* spectrum extracted with 25'' aperture represented 62% (70%) of the *XMM-Newton* soft (hard) emission (Table 7). When the contribution from the annular region was taken into account, the simultaneous fit resulted in variations of N_{H2} (93%) and $Norm_2$ (57%), with 37% (81%) variations in the soft (hard) energies in one year period (Table 8).

We analyzed short time scale variability from individual light curves, by calculating χ^2 and σ^2 (see Table 9 and Figure C.2 (up)). Data from 2006 showed $\chi_r^2 = 4.7$ and a normalized excess variance $\sigma_{NXS} = 1.8 \pm 0.1 \times 10^{-2}$ indicating variability (see Figure C.2, upper-right). However, NGC 3227 is a strong variable Seyfert 1 located 2' from NGC 3226. Thus, we analyzed the possibility that NGC 3226 was contaminated by its emission. We extracted a light curve from NGC 3227 and from a circular region between both galaxies close to NGC 3226 (background), and the same pattern of variability was found. In Figure C.2 we present the light curves for the background (middle-left) and NGC 3227 (middle-right), and the *XMM-Newton* image (down). The normalized excess variance for the background light curve was $\sigma_{NXS} = 1.5 \pm 0.5 \times 10^{-2}$. Therefore, we conclude that NGC 3226 might be contaminated by emission from NGC 3227, so its short time scale variability cannot be assessed. Only UVW1 observations are available from OM (see Table 10 and Figure 2), with a 10-12 % variation (7.4σ).

5.1.3. NGC 3627

We used one *XMM-Newton* observation in May 2001 and another *Chandra* observation in March 2008 (see Table 2). We re-

call that different apertures (8" for *Chandra* and 25" for *XMM-Newton*) were used for the extraction of the nuclear spectrum.

Since observations were obtained with different instruments, comparisons of HR were avoided.

According to χ_r^2 , both spectra were individually best-fitted with a MEPL model. The best simultaneous fit implied variations in N_{H2} (Figure 1), from no absorption to $N_{H2} = 1.28 \times 10^{22} \text{cm}^{-2}$ in a 7 year period (i.e. SMF1, Table 5). Even if observed fluxes vary, when computing intrinsic luminosities (see Table 6) for this model we get variations below 1σ in the soft and the hard energies, indicating no variations in 7 years (Figure 2).

To compare *Chandra* and *XMM-Newton* data, we carried out the analysis explained in Sect. 4.2.1. The contribution of the annular region to the 25" aperture *Chandra* spectrum is $\sim 92\%$ in the 0.5-10 keV band (see Table 7). Thus we assumed that *XMM-Newton* data were strongly contaminated by emission surrounding the nucleus, which avoided the joint use of *Chandra* and *XMM-Newton* data for this object (see Section 4.2.1).

The analysis of the light curves did not show short time scale variability (see Table 9 and Figure C.3), since all measures were below 2σ from the average.

5.1.4. NGC 4261

We used two *Chandra* (May 2000 and February 2008) and two *XMM-Newton* observations (December 2001 and December 2007) for this object. Given the different resolutions in both sets of observations we firstly performed the analysis separately (see Table 2).

Variations of 19% and 0% in HR were obtained for *Chandra* and *XMM-Newton*, respectively (from Column 8 in Table 2).

The best fit for the *Chandra* spectra is a ME2PL model from the individual analysis. The simultaneous fit without allowing to vary any parameter (i.e. SMF0) resulted in a good fit ($\chi^2/d.o.f = 1.27$). Varying one parameter did not give an improvement in the final fit. Therefore, the source seemed to be non-variable (see Table 5 and Figure 1). X-ray luminosity variations were below 1σ for the soft and the hard bands over a period of 8 years (Table 6 and Figure 2).

The individual analysis of the two observations with *XMM-Newton* again gave as a best fit the ME2PL model, and variations in the parameters did not improve the fit (i.e. the best fit was SMF0). Thus, we obtained a non-variable source (Table 5 and Figure 1). X-ray luminosity variations were below 1σ in a 6 year period in this case (Table 6 and Figure 2).

To compare data from *Chandra* and *XMM-Newton*, the procedure explained in section 4.2.1 was applied to this object. We compared obsID 9569 from *Chandra* and obsID 0502120101 from *XMM-Newton* data (Figure B.1) since they are the closest in time. The contribution of the emission from the annular region was 37% in the 0.5-10 keV band emission in the 25" aperture *Chandra* data. Intrinsic luminosities of the 25" aperture *Chandra* spectrum represented 37% (66%) of the soft (hard) emission from *XMM-Newton* data. The simultaneous fit between these data taking into account the annular contribution resulted in a non-variable object (Table 8).

To check for short time scale variability we analyzed the light curves for each observation (see Table 9 and Figure C.4). No short time variability was detected for this object, since all measurements were below 2σ from the average.

Considering the UV range (Table 10), the variations amounted to 9-11 % (10.3σ) in the UVW1 filter and 28-39 % (9.3σ) in the UVM2 filter (see Figure 2).

5.1.5. NGC 4278

We only used three of the nine observations taken by *Chandra*, in March 2006, February 2007 and April 2007, and the *XMM-Newton* observation in May 2004 (Table 2).

HR variations amounted to 4% for the runs with useful spectroscopic *Chandra* data. Taking into account all the observations from *Chandra*, 40% HR variations were found between 2000 and 2010 (from Column 8 in Table 2).

Our best fit for *Chandra* data was a MEPL model with $Norm_2$ varying (i.e. SMF1, see Figure 1). This parameter varied 30% between the first and the last observation (≈ 1 year apart) (Table 5). X-ray intrinsic luminosity variations (Table 6) were within 11.2σ (9.6σ) for the soft (hard) energies. This corresponded to variation amplitudes of 26% (29%, see Figure 2). It is remarkable that flux variations were 11% (13%) between the second and the third observations (two months apart), with a 13% variation in $Norm_2$ for the same period (Tables 5 and 6).

We compared the *XMM-Newton* observation in 2004 with the *Chandra* observation in 2006, which is the closest in time (see Figure B.1). We applied the procedure explained in section 4.2.1. The spectral analysis of *XMM-Newton* spectrum, included in Tables 5 and 6, gave a PL as the best fit model. The contribution of the annular region is 38% in the 0.5-10.0 keV band to the emission in the 25" aperture *Chandra* data. The *Chandra* spectrum extracted with 25" aperture represented 25% (20%) of the soft (hard) *XMM-Newton* emission. When the contribution of the annular region was taken into account, the resulting Γ was in agreement with that from *XMM-Newton* data (see Table 7). The simultaneous fit shows 15% of variations in the normalization of the PL along two years (Table 8).

The analysis of the light curves (see Table 9 and Figure C.5) did not show short time scale variability, either in *Chandra* or in *XMM-Newton* data.

5.1.6. NGC 4552

We used a *Chandra* observation taken in April 2001 and a *XMM-Newton* observation taken in July 2003. We recall that different apertures were used (3" for *Chandra* and 25" for *XMM-Newton* data).

Since observations were obtained with different instruments, comparisons of HR were avoided.

Both observations needed MEPL for the individual best fit. When varying parameters, the best fit was obtained when $Norm_1$ and $Norm_2$ varied (i.e. SMF2, $\chi_r^2=1.21$, see also Figure 1), with 93% and 78% amplitude variations (see Table 5). We found intrinsic luminosity variations at 21.5σ (14.1σ) in the soft (hard) energies, i.e., 87% (79%) amplitude variations in a period of two years (Table 6).

The *Chandra* image of this object revealed many X-ray sources surrounding the nucleus (see Figure B.1). The contribution of the annular region to the 0.5-10.0 keV band emission in the 25" aperture *Chandra* data was 23%. Extraction from *Chandra* data with 25" aperture resulted in a 72% (60%) emission of the soft (hard) *XMM-Newton* data. The simultaneous fit resulted in a variable object, where $Norm_1$ (21%) and $Norm_2$ (37%) varied, with 29% (37%) flux variations in the soft (hard) energies (see Figure 2 and Table 8).

Short time scale variations were not found (see Table 9 and Figure C.6).

5.1.7. NGC 5846

We used two observations from *XMM-Newton* (January and August 2001) and other two observations from *Chandra* (May 2000 and June 2007). The analysis was firstly made separately due to different apertures (see Table 2).

HR Variations of 1% and 6% were obtained for *XMM-Newton* and *Chandra* data, respectively (from Column 8 in Table 2).

In the case of *Chandra* observations, we only made the analysis up to 3 keV, due to low count-rate at hard energies. In this case SMF0 was used, resulting in a non-variable source when fitting a MEPL model (Table 5 and Figure 1) with flux variations below 1σ in a period of 7 years (Table 6 and Figure 2). The *XMM-Newton* data did not show variability (the best fit model is MEPL, see Table 5 and Figure 1), and flux variations below 1σ on the soft and hard energies for a period of 7 months (Table 6).

The contribution to the 0.5-10.0 keV band emission from the 25" aperture *Chandra* data was 73% from the annular region, what avoided the joint use of *Chandra* and *XMM-Newton* data for this object. No short time scale variability was found for this object (see Table 9 and Figure C.7). The availability of UV data for a single epoch precludes any attempt to get information on its variability.

5.2. Spectral variability

A rough description of the spectral shape is provided by HR. Consequently, a first approximation of the spectral variations can be obtained from the variation of HR. The use of HR allows the inclusion of observations for which the number of counts are not enough for a proper spectral fitting. Note that, since the calculation of HR is based on number counts, we only used data coming from the same instrument for comparisons. We considered that variations greater than 20% (2σ error) in HR may correspond to variable objects (NGC 1052, NGC 3226, and NGC 4278). Note that variations in HR smaller than 20% can be found in variable objects, since the variations in soft and hard energies may have different signs and somewhat compensate in the final calculation of HR.

The individual fitting of each observation revealed that composite models (2PL, MEPL or ME2PL) were needed in all cases. A thermal component was used in six objects, all of them with $kT \approx 0.60$ keV.

We fitted all available data, for the same object and model, varying different parameters to get information on the variability pattern. Fig. 1 shows the best fit (top panel) with the residuals of the individual observations (bottom panels). In order to analyze the data from *Chandra* and *XMM-Newton* data jointly, we estimated the influence of extra-nuclear emission on the results (see Section 4.2.1). For two objects (NGC 3627 and NGC 5846) the contamination by emission surrounding the nucleus in *XMM-Newton* data was so high (up to 50%) that we avoided the comparisons in these cases. For the remaining five sources (NGC 1052, NGC 3226, NGC 4261, NGC 4278, and NGC 4552), the joint analysis was attempted.

Two objects are compatible with being non-variable sources, namely NGC 4261 and NGC 5846. For these two objects the same conclusion is reached if we isolate the analysis of *Chandra* and *XMM-Newton* data, both with similar spectral parameters (see Table 5). Moreover, NGC 3627 was not longer used for further discussion, since contamination prevents of any variability analysis. Four objects are variable, namely NGC 1052, NGC 3226, NGC 4278, and NGC 4552. NGC 1052

and NGC 3226 showed variations in N_{H2} (31% and 93%) and $Norm_2$ (49% and 57%) (in eight and one years), while NGC 4278 showed changes in $Norm_2$ (30%) (in three years). NGC 4552 showed variations in $Norm_1$ (21%) and $Norm_2$ (37%) in a two years period. All the variations occur at hard energies, and these variations are related to the absorber and/or to the nuclear power. Even if the small number of sources precludes any statistical characterization, there does not seem to exist any clear relation with either the LINER type (1 or 2) or to the Eddington ratios (see Table 11). A larger sample of LINERs is needed to search for any variability pattern to be eventually more frequently observed than others.

5.3. Flux variability

X-ray soft and hard luminosities (see Table 6) are shown in Figure 2. Two objects are compatible with no variations of the central engine (NGC 4261, and NGC 5846). Four sources are compatible with being variable, NGC 1052 with 20% variations in both bands, NGC 3226 with 37% (81%) variations in the soft (hard) band, NGC 4278 with 26% (29%) variations in the soft (hard), and NGC 4552 with 29% (37%) variations in the soft (hard) band. Sources showing flux variability in the soft and hard bands also showed spectral variability (see Sec. 5.2).

We also studied the UV variability for the sources, by studying UV and X-ray data obtained simultaneously with *XMM-Newton* (available for three galaxies). All of them are variable at UV frequencies (see Table 10 and Fig. 2). *XMM-OM* provided UV fluxes at three epochs for NGC 1052; $\sim 20\%$ variations were obtained with the filters UVW2 and UVM2. NGC 3226 was observed with the filter UVW1, showing 11% variation. NGC 4261 was observed with the filters UVW1 and UVM2, with 10% and 33% variations, respectively. Two objects, namely NGC 1052 and NGC 3226, showed UV and spectral variability, while another one, NGC 4261, showed UV variability but not spectral variability.

5.4. Light curves

Table 9 provides the values for χ_r^2 (and the probability of variability) and the σ_{NXS}^2 . Objects are considered to be variable when the count rates are different 3σ from the average. No short term variability (from hours to days) was found in our sample¹⁰.

6. Discussion

We have performed an X-ray spectral analysis to search for variability in seven LINER nuclei, three type 1.9 (NGC 1052, NGC 3226, and NGC 4278) and four type 2 (NGC 3627, NGC 4261, NGC 4552, and NGC 5846). We used data from *Chandra* and *XMM-Newton* satellites with observations at different epochs. Whenever possible, we made the analysis separately for each instrument to avoid corrections due to different apertures. The results obtained for the long term variability of NGC 3627 will not be used for further discussion (see Section 5.1.3).

Our main results are:

- Short term variability: No variations were found on time scales from hours to days.

¹⁰ Note that we do not take into account obsID 0400270101 from NGC 3226 (see Section 5.1.2).

- Long term variability: Four out of the six objects (NGC 1052, NGC 3226, NGC 4278, and NGC 4552) were variable in X-rays on time scales from months to years. The shortest variation is found for NGC 4278 in time scales of two months. Simultaneous observations in the UV for three objects (NGC 1052, NGC 3226, and NGC 4261) revealed variations on time scales of years.
- Main driver for the variability: Among the variable sources, NGC 4278 presented variations in Norm₂, NGC 4552 in Norm₁ and Norm₂, and NGC 1052 and NGC 3226 in N_{H2} and Norm₂. In all the variable LINERs variations occur at hard energies.

6.1. Short and long time scale variability

In our sample of LINERs we analyzed variability from hours to days (short term) from the analysis of the light curves for each observation (see Col. 6 in Table 2), and from months to years (long term) from the simultaneous fitting of the different observations (see Col. 10 in Table 11).

Concerning short time-scales, Pian et al. (2010) studied four type 1 LINERs and found variations of 30% in a half a day in NGC 3998, and 30% variations in the hard (1-10 keV) X-rays in ~ 3 hours in M 81. The other two sources in their sample (NGC 4203 and NGC 4579) did not show short time scale variability. The power spectral density (PSD) profiles of the 14 LINERs included in the sample of 104 AGN in González-Martín & Vaughan (2012), did not show short-term variability except for two objects (3C218 and NGC 3031). All these studies suggest that about 20% of LINERs show short time-scale variability. This percentage goes to zero in our own study, since none of our seven sources showed short time scale variability, according to the χ^2_r and the normalised excess variance, σ^2_{NXS} , (see Table 9). Younes et al. (2010) found variability in ~ 1.5 hours for NGC 4278 on the *XMM-Newton* observation, where the flux increased 10%. Using the same observation we found a 3% flux increase in the same period, and a null probability of being a variable source. The difference is most probably due to the different apertures used in the analysis. Adding up all the studied LINERs from this and previous papers, the percentage of variable LINERs at short time-scales is 16%.

Long term spectral variability is clearly found for four objects in our sample. NGC 1052 needed variations in N_{H2} (49%) and Norm₂ (31%) in a period of eight years, NGC 3226 also varied N_{H2} (93%) and Norm₂ (57%) in a period of one year, NGC 4278 varied Norm₂ (30%) in a period of one year, and NGC 4552 varied Norm₁ (21%) and Norm₂ (37%) in two years.

Long term variability is common among LINERs. Younes et al. (2011) studied a sample of type 1 LINERs, where seven out of nine sources showed long term variability (i.e. months and/or years). Two of their objects are in common with our sample, namely NGC 3226 and NGC 4278. We found similar spectral characteristics and the same parameters varying for both objects. In the case of NGC 3226, they found that the N_H varied 72% and Norm varied 48% when fitting a simple power law. This is similar to our results, although we used two absorbers instead of one. They found flux variations of 49% (46%) in the soft (hard) band between the *Chandra* and *XMM-Newton* observations, while we found 37% (81%), the differences most probably due to the different models used. In the case of NGC 4278 they used seven public observations from the archive, while we only used three. Despite this, the same spectral variation was found (Norm₂). Younes et al. (2010) found for NGC 4278 a 31% (20%) variation at soft (hard)

energies, where we found 26% (29%) variation for the same observations. Pian et al. (2010) found long term variability in two of their four type 1 LINERs using *Swift* data. Therefore, long term variability is found in $\sim 65\%$ of the LINERs, significantly larger than that of LINERs at short time scales.

Three kinds of long term X-ray variability patterns have been found in our sample: (1) variations in the soft excess (NGC 4552); (2) variations of the obscuring matter (NGC 1052 and NGC 3226); and (3) variations of the intrinsic source (NGC 1052, NGC 3226, NGC 4278, and NGC 4552). As in the case of NGC 4552, variations at soft energies has already been reported in the literature for the type 2 LINER NGC 4102 (González-Martín et al. 2011a). This behaviour is seen in type 1 Seyferts, where absorption variations are related to a partially ionized, optically thin material along the line of sight to the central source, the so called warm absorber (Reynolds 1997; Petrucci et al. 2013). The variations due to the N_H of the X-ray absorbing gas that we see in two sources are well established for many famous type 2 Seyferts. These variations are thought to be related to the motion of clouds perpendicular to the line of sight of the observer to the AGN. These clouds produce partial eclipses of the AGN over time. In some cases, the fast movement of the clouds places them at the distance of the BLR, although in other cases the clouds seem to be located at further distances (few parsecs) from the AGN (e.g. NGC 1365 Risaliti 2002; Risaliti et al. 2007, 2010; Braito et al. 2013). The time scale of the N_H variations in our sample are consistent with this latter scenario. The most common pattern of variability among the LINERs in our sample (four cases) is the change on the intrinsic continuum of the source. McHardy et al. (2006) found that the time scale of the intrinsic variability increases for larger masses of the black hole and/or lower bolometric luminosities for objects where variability is related to the nuclear power¹¹. According to the revised relation between the BH mass, bolometric luminosities and time scales of variations, González-Martín & Vaughan (2012) predicted that LINERs (with M_{BH} $\sim 10^{8-9}M_{\odot}$) do not vary in time scales lower than tens of days. Applying their formula to our four objects, predicted values for NGC 1052, NGC 3226, NGC 4278, and NGC 4552 were 13.3, 28.2, 118.0 and 449.9 days (see Table 11 for the values of M_{BH} and L_{bol}), that is, time scales of days, months and years were expected for these objects. This is in agreement with our results for NGC 4278 and NGC 4552. Unfortunately, we do not have observations within days for NGC 1052 and NGC 3226, we were only able to search for variations on time scales from months to years. Moreover, in the cases of NGC 1052, NGC 3226, and NGC 4552 coupled variations¹² were obtained. A study of a larger sample of LINERs will be required to constrain the time scale of the intrinsic variability for these sources and be able to understand whether LINERs match in the same scenario than more powerful AGN.

A first approximation of the variations can be obtained by the analysis of the hardness ratios. We have considered differences in HR larger than 20% as a measure of spectral variation. For NGC 1052, HR varied 33% between the first and last *XMM-Newton* observations and no variation is found for HR over the 5 year period observed by *Chandra*. These results are compatible with flux variations obtained when analyzing *XMM-Newton* data. NGC 3226 presents HR differences over 100% in *Chandra*

¹¹ Although the dependence on the bolometric luminosity does not seem to be so strong according to González-Martín & Vaughan (2012)

¹² Variations are needed for more than one parameter in the spectral fitting

data. For NGC 4278 total HR variations amount to 40% when using all the *Chandra* available data, although the results from the *Chandra* data used for spectral analysis appear to be compatible with no variations. NGC 4261 and NGC 5846 are compatible with being non-variable objects, both with *XMM-Newton* and *Chandra* data, and with both analyses, spectroscopic and HR. NGC 4261 shows HR differences of 19%, which seem to be compatible with the flux variations obtained through the individual analysis of the source.

Variability among LINERs is not restricted to X-rays. The work done by Maoz et al. (2005) was the first to show variability at UV frequencies in LINER galaxies, where all but three objects in their sample of 17 LINERs 1 and 2 were variable. From the literature, we found different studies for the LINERs in our sample using *HST* data (see Appendix A for details). Cappellari et al. (1999) studied FOC data for NGC 4552, and found a factor 4.5 brightening between 1991 and 1993 (filter F342W), followed by a factor ~ 2 dimming between 1993 and 1996 (filters F175W, F275W and F342W). Maoz et al. (2005) studied both NGC 1052 and NGC 4552, concluding that both of them were variable on time scales of years. NGC 4278 was studied by Cardullo et al. (2008), who found a luminosity increase of a factor 1.6 over 6 months. UV data were not available for the remaining two objects in our sample (NGC 3627 and NGC 5846). Thus, from the seven LINERs in our sample five seem to be variable at UV frequencies. Simultaneous X-rays and UV data were obtained from *XMM-Newton* data for three objects (NGC 1052, NGC 3226, and NGC 4261), all showing variability, whereas intrinsic variations in X-rays are not found for NGC 4261. A possible explanation for this source to the non-simultaneous X-ray and UV variation could be the existence of time lags in both frequencies. Time lag explanations has already been reported for the NLSy1 galaxy NGC 4051 by Alston et al. (2013). Repeated, simultaneous observations at X-rays and UV frequencies would be required for verifying this model.

6.2. Accretion mechanism

It has been suggested in the literature that the accretion mechanism in low luminosity active galactic nuclei (LLAGN) is different from that in more powerful AGN (e.g. Seyferts), and more similar to that in X-Ray Binaries (XRB) in their low/hard state (Yamaoka et al. 2005; Yuan et al. 2007; Gu & Cao 2009; Younes et al. 2011; Xu 2011). The X-ray emission is supposed to originate from the Comptonization process in advection dominated accretion flow (ADAF), where accretion is inefficient for $L_{\text{bol}}/L_{\text{Edd}} < 10^{-3}$. At low accretion rates, the infalling material may never cool sufficiently to collapse into a thin disk (as is the case for efficient radiation), and an advection-dominated flow from the outermost radius down to the black hole could be formed (Narayan & Yi 1994). In powerful AGN a positive correlation between the hard X-ray photon index, Γ , and the Eddington ratio, $L_{\text{bol}}/L_{\text{Edd}}$ was found by Shemmer et al. (2006), who argued that the hard X-ray photon index depends primarily on the accretion rate. On the contrary, according to the results provided by Mahadevan (1997), the lower the accretion rate, the less efficient is the cooling by comptonization and the X-ray region of the spectrum becomes softer and reaches lower luminosities. In this case a negative correlation between these magnitudes has been found for LLAGN (Gu & Cao 2009; Younes et al. 2011), and also for XRB. We present these parameters for each individual observation in our sample of LINERs in Figure 3, where the negative correlation is shown. $\log(L_{\text{bol}}/L_{\text{Edd}})$ were calculated following the formula-

tion given in Eracleous et al. (2010b), using $L_{\text{bol}} = 33L_{2-10\text{keV}}$. We corrected the equation given by Younes et al. (2011) by this factor (they used $L_{\text{bol}} = 16L_{2-10\text{keV}}$) and plotted it as a solid line. Our results are consistent with the correlation given by Younes et al. (2011) for their sample of type 1 LINERs. Emmanoulopoulos et al. (2012) found for the first time a ‘harder when brighter’ (i.e. higher luminosities for harder spectra) X-ray behaviour for the LLAGN NGC 7213, where they found variations in Γ . However, we did not find this behaviour for any of the sources in our sample, Figure 3 showing the consistency of our simultaneous fittings with no variations in Γ .

We also computed the X-ray to UV flux ratio, α_{ox} (see Section 4.3.2). We calculated these values for all sources with simultaneous observations at X-ray and UV (see Table 10), obtaining values of α_{ox} between $[-0.81, -1.66]$, in good agreement with previous studies (Maoz 2007; Younes et al. 2012). Despite being similar to the α_{ox} given for powerful AGN, these values were slightly lower (Maoz 2007). This may indicate the lack or absence of the ‘big blue bump’.

In the cases where α_{ox} could be calculated more than once (NGC 1052 and NGC 4261) no variations were found within the errors.

Another indication of a different emission process between powerful AGN and LINERs could be the positive correlation found by Younes et al. (2012) between α_{ox} and $\log(L_{\text{bol}}/L_{\text{Edd}})$, in contrast with the anticorrelation found for powerful AGN. In order to compare the results from Younes et al. (2012) and ours, we recalculated $\log(L_{\text{bol}}/L_{\text{Edd}})$ for the sample in Younes et al. (2012) following the relation given by Eracleous et al. (2010b) and using the data from Younes et al. (2011). In Fig. 4 we plot this relation (see Table 10), where the symbols used for the sources from Younes et al. (2012) are stars. The results are in good agreement, indicating a correlation between α_{ox} and $\log(L_{\text{bol}}/L_{\text{Edd}})$. Younes et al. (2012) suggested that this behaviour can be understood within the framework of radiatively inefficient accretion flow models, such as ADAF.

7. Conclusions

A spectral variability analysis of seven LINER nuclei was performed using public data from *Chandra* and *XMM-Newton*. The main conclusions of this paper can be summarized as follows:

1. Variations greater than 20% in the hardness ratio always correspond to objects showing spectral variability.
2. Individual fits of each observation provided composite models as the best fit (2PL, MEPL, and ME2PL).
3. No short time scale variability was found, in agreement with predictions.
4. Spectral X-ray variability was found in four out of six objects. In all of them variations occurred at hard energies due to the absorber and/or the nuclear source, and variations in the soft energy were found only in NGC 4552. These variations occur on time scales of months and/or years. The shortest time scale was found for NGC 4278, with variations of two months.
5. We found an anticorrelation between the X-ray spectral index, Γ , and the Eddington ratio, $L_{\text{bol}}/L_{\text{Edd}}$. We have also found a correlation between the X-ray to UV flux ratio, α_{ox} , and the Eddington ratio, $L_{\text{bol}}/L_{\text{Edd}}$. Both relations are compatible with inefficient flows being the origin of the accretion mechanism in these sources.

Acknowledgements. We thank the anonymous referee for his/her helpful comments that helped to improve the paper, T. Mahoney for reviewing the English,

J. Perea for help with the statistical analysis and the AGN group at the IAA for helpful comments during this work. This work was financed by MINECO grant AYA 2010-15169, Junta de Andalucía TIC114 and Proyecto de Excelencia de la Junta de Andalucía P08-TIC-03531. LHG acknowledges financial support from the Ministerio de Economía y Competitividad through the Spanish grant FPI BES-2011-043319. OGM thanks Spanish MINECO through a Juan de la Cierva Fellowship. This research made use of data obtained from the *Chandra* Data Archive provided by the *Chandra* X-ray Center (CXC). This research made use of data obtained from the *XMM-Newton* Data Archive provided by the *XMM-Newton* Science Archive (XSA). This research made use of the NASA/IPAC extragalactic database (NED), which is operated by the Jet Propulsion Laboratory under contract with the National Aeronautics and Space Administration.

References

- Alston, W. N., Vaughan, S., & Uttley, P. 2013, *MNRAS*, 429, 75
- Antonucci, R. 1993, *ARA&A*, 31, 473
- Binder, B., Markowitz, A., & Rothschild, R. E. 2009, *ApJ*, 691, 431
- Birkinshaw, M. & Davies, R. L. 1985, *ApJ*, 291, 32
- Boroson, B., Kim, D.-W., & Fabbiano, G. 2011, *ApJ*, 729, 12
- Box, G. E. P. 1953, *Biometrika*, 40, 318
- Braitto, V., Ballo, L., Reeves, J. N., et al. 2013, *MNRAS*, 428, 2516
- Brassington, N. J., Fabbiano, G., Kim, D.-W., et al. 2009, *ApJS*, 181, 605
- Brenneman, L. W., Weaver, K. A., Kadler, M., et al. 2009, *ApJ*, 698, 528
- Brightman, M. & Nandra, K. 2011, *MNRAS*, 413, 1206
- Caballero-García, M. D., Papadakis, I. E., Nicastro, F., & Ajello, M. 2012, *A&A*, 537, A87
- Cappellari, M., Renzini, A., Greggio, L., et al. 1999, *ApJ*, 519, 117
- Cardullo, A., Corsini, E. M., Beifiori, A., Pizzella, A., & Buson, L. M. 2008, in *Astronomical Society of the Pacific Conference Series*, Vol. 396, *Formation and Evolution of Galaxy Disks*, ed. J. G. Funes & E. M. Corsini, 53
- Carollo, C. M., Franx, M., Illingworth, G. D., & Forbes, D. A. 1997, *ApJ*, 481, 710
- Dickey, J. M. & Lockman, F. J. 1990, *ARA&A*, 28, 215
- Donato, D., Sambruna, R. M., & Gliozzi, M. 2004, *ApJ*, 617, 915
- D’Onofrio, M., Marziani, P., & Sulentic, J. W. 2012, *Fifty Years of Quasars: Current Impressions and Future Perspectives*, ed. M. D’Onofrio, P. Marziani, & J. W. Sulentic, 549
- Dopita, M. A. & Sutherland, R. S. 1995, *ApJ*, 455, 468
- Dudik, R. P., Satyapal, S., Gliozzi, M., & Sambruna, R. M. 2005, *ApJ*, 620, 113
- Emmanoulopoulos, D., Papadakis, I. E., McHardy, I. M., et al. 2012, *MNRAS*, 424, 1327
- Eracleous, M., Hwang, J. A., & Flohic, H. M. L. G. 2010a, *ApJS*, 187, 135
- Eracleous, M., Hwang, J. A., & Flohic, H. M. L. G. 2010b, *ApJS*, 187, 135
- Evans, D. A., Hardcastle, M. J., Croston, J. H., Worrall, D. M., & Birkinshaw, M. 2005, *MNRAS*, 359, 363
- Ferrarese, L., Ford, H. C., Huchra, J., et al. 2000, *ApJS*, 128, 431
- Ferrarese, L., Ford, H. C., & Jaffe, W. 1996, *ApJ*, 470, 444
- Filho, M. E., Fraternali, F., Markoff, S., et al. 2004, *A&A*, 418, 429
- Garmire, G. P., Bautz, M. W., Ford, P. G., Nousek, J. A., & Ricker, J. G. R. 2003, in *Society of Photo-Optical Instrumentation Engineers (SPIE) Conference Series*, Vol. 4851, *Society of Photo-Optical Instrumentation Engineers (SPIE) Conference Series*, ed. J. E. Truemper & H. D. Tananbaum, 28–44
- George, I. M., Mushotzky, R. F., Yaqoob, T., et al. 2001, *ApJ*, 559, 167
- Gliozzi, M., Sambruna, R. M., & Brandt, W. N. 2003, *A&A*, 408, 949
- Gondoin, P., Orr, A., & Siddiqui, H. 2004, *A&A*, 420, 905
- González-Martín, O., Masegosa, J., Márquez, I., & Guainazzi, M. 2009a, *ApJ*, 704, 1570
- González-Martín, O., Masegosa, J., Márquez, I., Guainazzi, M., & Jiménez-Bailón, E. 2009b, *A&A*, 506, 1107
- González-Martín, O., Papadakis, I., Braitto, V., et al. 2011a, *A&A*, 527, A142
- González-Martín, O., Papadakis, I., Reig, P., & Zezas, A. 2011b, *A&A*, 526, A132
- González-Martín, O. & Vaughan, S. 2012, *A&A*, 544, A80
- Grier, C. J., Mathur, S., Ghosh, H., & Ferrarese, L. 2011, *ApJ*, 731, 60
- Gu, M. & Cao, X. 2009, *MNRAS*, 399, 349
- Guainazzi, M., Matt, G., & Perola, G. C. 2005, *A&A*, 444, 119
- Heckman, T. M. 1980, *A&A*, 87, 152
- Ho, L. C. 2008, *ARA&A*, 46, 475
- Ho, L. C., Feigelson, E. D., Townsley, L. K., et al. 2001, *ApJ*, 549, L51
- Ho, L. C., Filippenko, A. V., & Sargent, W. L. W. 1993, *ApJ*, 417, 63
- Ho, L. C., Filippenko, A. V., Sargent, W. L. W., & Peng, C. Y. 1997, *ApJS*, 112, 391
- Kalberla, P. M. W., Burton, W. B., Hartmann, D., et al. 2005, *A&A*, 440, 775
- Krolik, J. H. 1999, *Active galactic nuclei : from the central black hole to the galactic environment*
- Mahadevan, R. 1997, *ApJ*, 477, 585
- Maoz, D. 2007, *MNRAS*, 377, 1696
- Maoz, D., Nagar, N. M., Falcke, H., & Wilson, A. S. 2005, *ApJ*, 625, 699
- Márquez, I. 2012, in *Fifty Years of Quasars: From Early Observations and Ideas to Future Research*, M. D’Onofrio and P. Marziani and J.W. Sulentic, *Astrophysics and Space Science Library* (Springer)
- Masegosa, J., Márquez, I., Ramirez, A., & González-Martín, O. 2011, *A&A*, 527, A23
- McHardy, I. M., Koerding, E., Knigge, C., Uttley, P., & Fender, R. P. 2006, *Nature*, 444, 730
- Moellenhoff, C., Hummel, E., & Bender, R. 1992, *A&A*, 255, 35
- Nagar, N. M., Falcke, H., & Wilson, A. S. 2005, *A&A*, 435, 521
- Narayan, R. & Yi, I. 1994, *ApJ*, 428, L13
- Panessa, F., Bassani, L., Cappi, M., et al. 2006, *A&A*, 455, 173
- Panessa, F., de Rosa, A., Bassani, L., et al. 2011, *MNRAS*, 417, 2426
- Peterson, B. M. 1997, *An Introduction to Active Galactic Nuclei*, ed. Peterson, B. M.
- Petrucchi, P.-O., Paltani, S., Malzac, J., et al. 2013, *A&A*, 549, A73
- Pian, E., Romano, P., Maoz, D., et al. 2010, *MNRAS*, 401, 677
- Pogge, R. W., Maoz, D., Ho, L. C., & Eracleous, M. 2000, *ApJ*, 532, 323
- Ptak, A., Yaqoob, T., Mushotzky, R., Serlemitsos, P., & Griffiths, R. 1998, *ApJ*, 501, L37
- Reynolds, C. S. 1997, *MNRAS*, 286, 513
- Rinn, A. S., Sambruna, R. M., & Gliozzi, M. 2005, *ApJ*, 621, 167
- Risaliti, G. 2002, *A&A*, 386, 379
- Risaliti, G., Elvis, M., Bianchi, S., & Matt, G. 2010, *MNRAS*, 406, L20
- Risaliti, G., Elvis, M., Fabbiano, G., et al. 2007, *ApJ*, 659, L111
- Risaliti, G., Maiolino, R., & Bassani, L. 2000, *A&A*, 356, 33
- Risaliti, G., Nardini, E., Salvati, M., et al. 2011, *MNRAS*, 410, 1027
- Sambruna, R. M., Gliozzi, M., Eracleous, M., Brandt, W. N., & Mushotzky, R. 2003, *ApJ*, 586, L37
- Satyapal, S., Dudik, R. P., O’Halloran, B., & Gliozzi, M. 2005, *ApJ*, 633, 86
- Satyapal, S., Sambruna, R. M., & Dudik, R. P. 2004, *A&A*, 414, 825
- Schmidt, M. 1963, *Nature*, 197, 1040
- Shemmer, O., Brandt, W. N., Netzer, H., Maiolino, R., & Kaspi, S. 2006, *ApJ*, 646, L29
- Strüder, L., Briel, U., Dennerl, K., et al. 2001, *A&A*, 365, L18
- Terashima, Y. & Wilson, A. S. 2003, *ApJ*, 583, 145
- Terlevich, R. & Melnick, J. 1985, *MNRAS*, 213, 841
- Tonry, J. L., Dressler, A., Blakeslee, J. P., et al. 2001, *ApJ*, 546, 681
- Trinchieri, G. & Goudfrooij, P. 2002, *A&A*, 386, 472
- Urry, C. M. & Padovani, P. 1995, *PASP*, 107, 803
- Vaughan, S., Edelson, R., Warwick, R. S., & Uttley, P. 2003, *MNRAS*, 345, 1271
- Veilleux, S. & Osterbrock, D. E. 1987, *ApJS*, 63, 295
- Xu, Y., Xu, H., Zhang, Z., et al. 2005, *ApJ*, 631, 809
- Xu, Y.-D. 2011, *ApJ*, 739, 64
- Yamaoka, K., Uzawa, M., Arai, M., Yamazaki, T., & Yoshida, A. 2005, *Chinese Journal of Astronomy and Astrophysics Supplement*, 5, 273
- Younes, G., Porquet, D., Sabra, B., et al. 2010, *A&A*, 517, A33
- Younes, G., Porquet, D., Sabra, B., & Reeves, J. N. 2011, *A&A*, 530, A149
- Younes, G., Porquet, D., Sabra, B., Reeves, J. N., & Grosso, N. 2012, *A&A*, 539, A104
- Yuan, F., Taam, R. E., Misra, R., Wu, X.-B., & Xue, Y. 2007, *ApJ*, 658, 282
- Zezas, A., Birkinshaw, M., Worrall, D. M., Peters, A., & Fabbiano, G. 2005, *ApJ*, 627, 711

Table 1. General properties of the sample galaxies. Names (Col. 1 and 2), right ascension (Col. 3), declination (Col. 4), redshift (Col. 5), distance (Col. 6), galactic absorption (Col. 7), apparent magnitude in the Johnson filter B (Col. 8), reddening (Col. 9) and galaxy morphological type (Col. 10).

Name	Other Name	RA	DEC	Redshift	Dist. (Mpc)	NH(Gal) (cm^{-2})	m_B	E(B-V)	Morph. Type
(1)	(2)	(3)	(4)	(5)	(6)	(7)	(8)	(9)	(10)
NGC 1052		02 41 04.80	+08 15 20.8	0.0049	19.41	0.0307	11.436	0.027	E
NGC 3226	UGC 5617	10 23 27.01	+19 53 54.7	0.0059	23.55	0.0214	12.339	0.023	E
NGC 3627	M 66	11 20 15.03	+12 59 29.6	0.00242	10.28	0.0243	9.735	0.033	SABb(s)
NGC 4261	UGC 7360	12 19 23.22	+05 49 30.8	0.00737	31.62	0.0155	11.35	0.018	E
NGC 4278	M 98	12 20 06.83	+29 16 50.7	0.00216	16.07	0.0177	11.042	0.029	E
NGC 4552	M 89	12 35 39.81	+12 33 22.8	0.0038	15.35	0.0257	10.67	0.041	E
NGC 5846	UGC 9705	15 06 29.29	+01 36 20.2	0.00622	24.89	0.0426	11.074	0.056	E

¹³All the distances from Tonry et al. (2001) except that for that NGC 3627, which was taken from Ferrarese et al. (2000).

Fig. 1. For each object, all X-ray spectra are plotted together in the first row. Best fits and their residuals are also shown, one row per observation from second row on. The legends contain the date (in the format yyymmdd) and the obsID. Details given in Table 2.

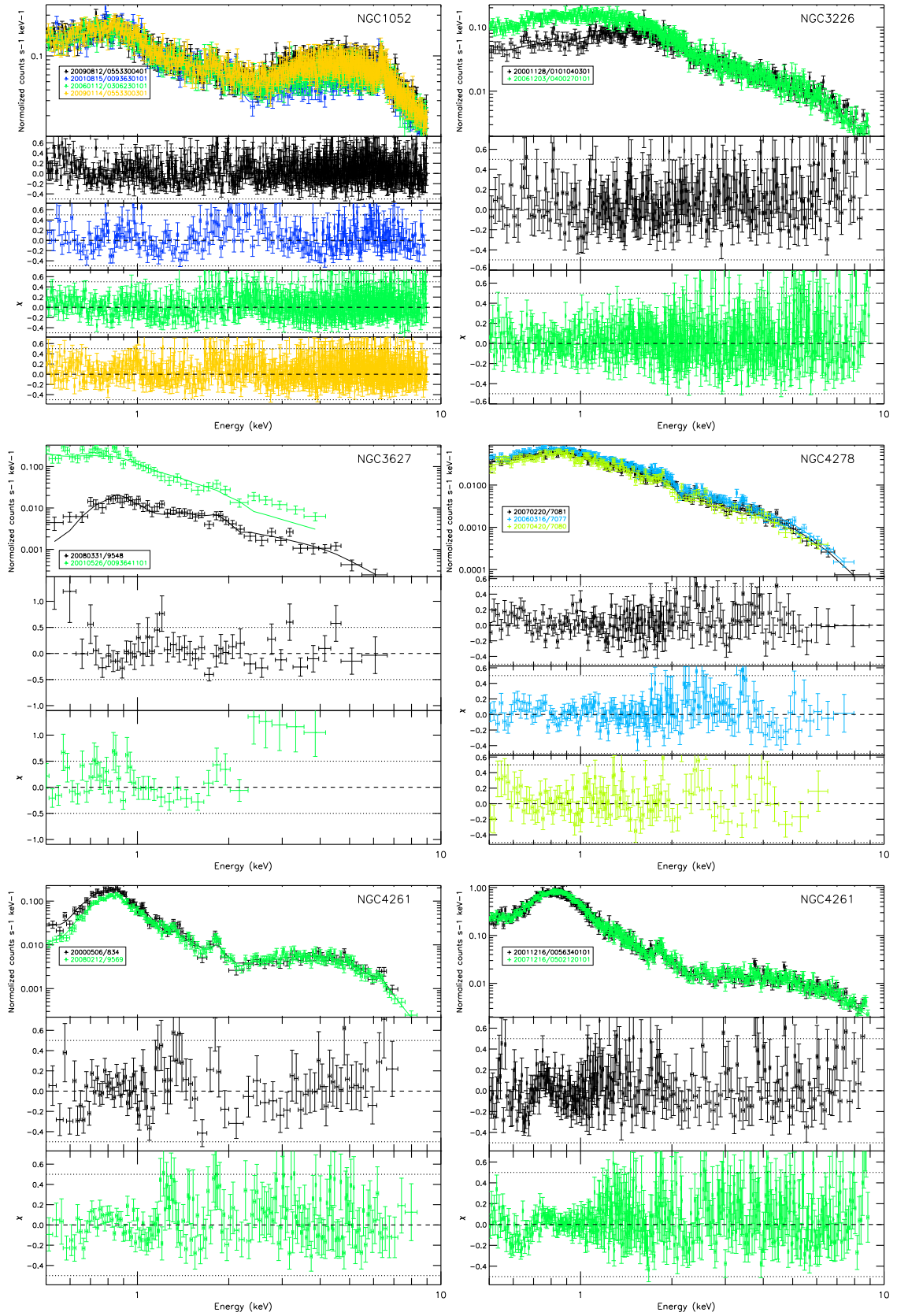


Fig. 1. Cont.

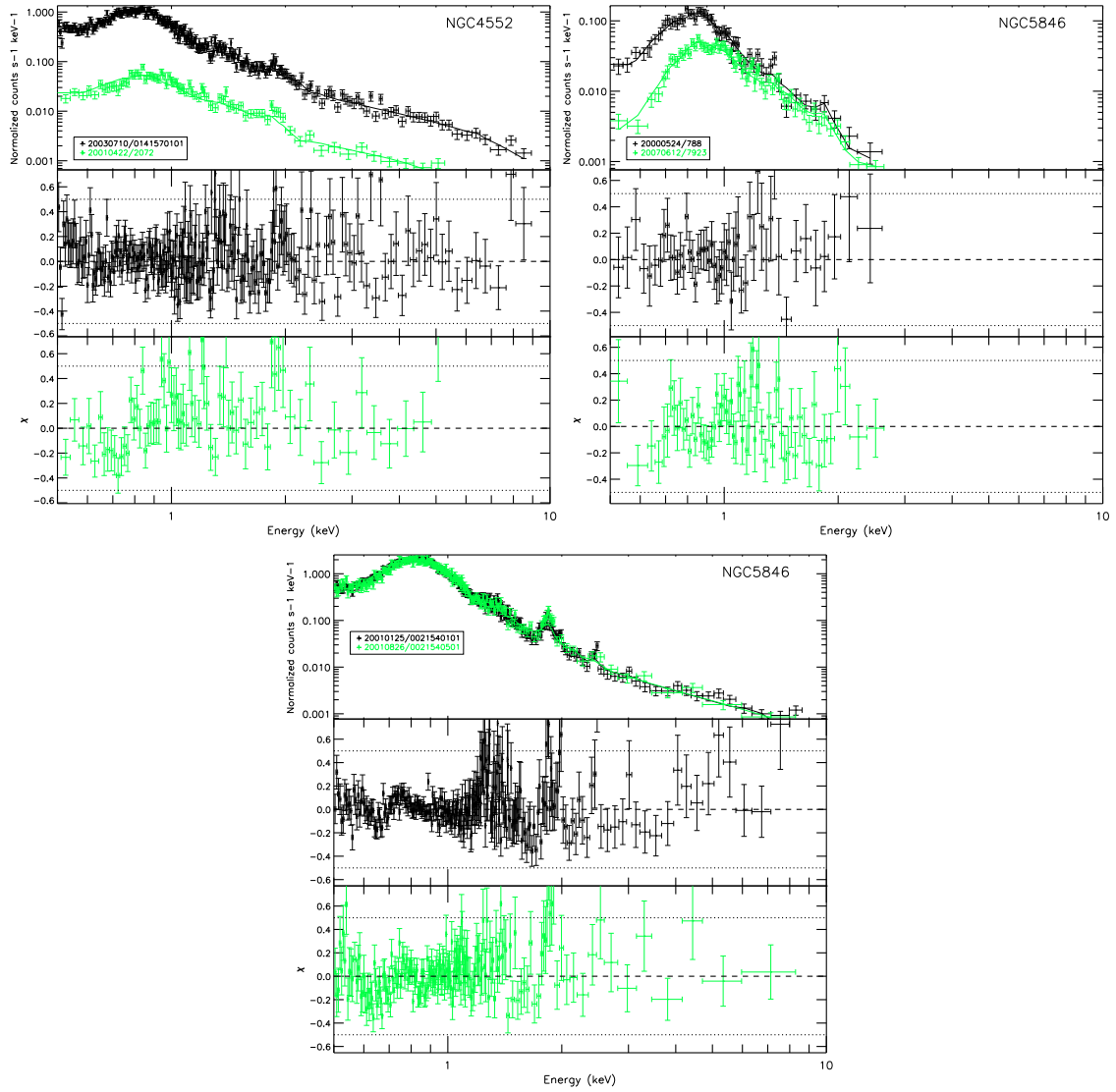


Fig. 2. Left: Intrinsic luminosities calculated for the soft (0.5–2.0 keV) and hard (2.0–10.0 keV) energies in the simultaneous fitting. Right: UV luminosities obtained from the data with the OM camera onboard *XMM-Newton*, when available.

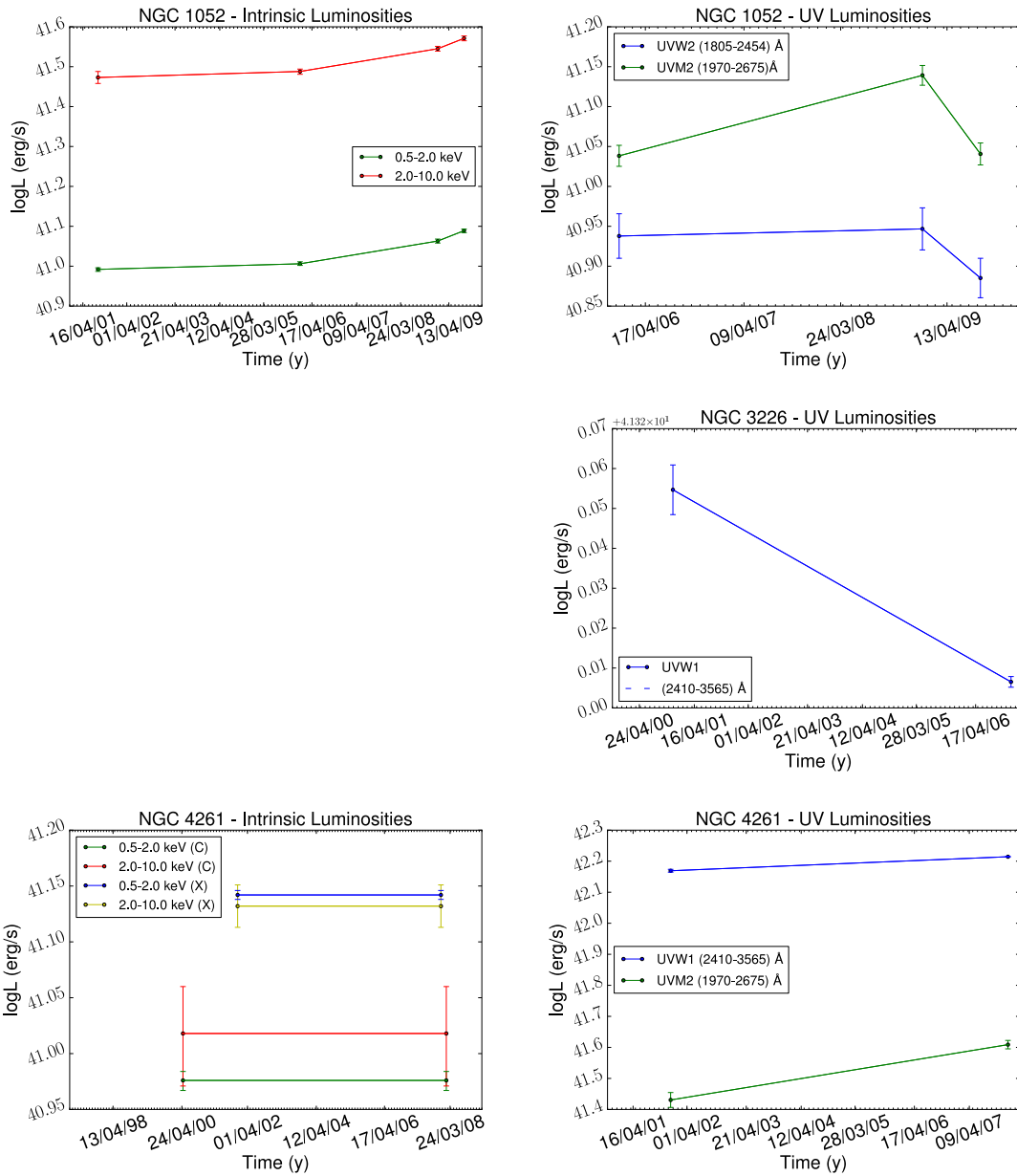


Fig. 2. Cont.

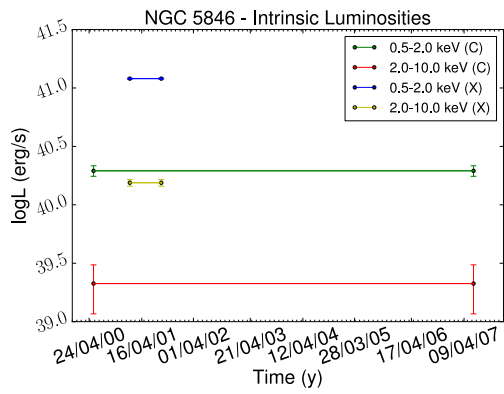
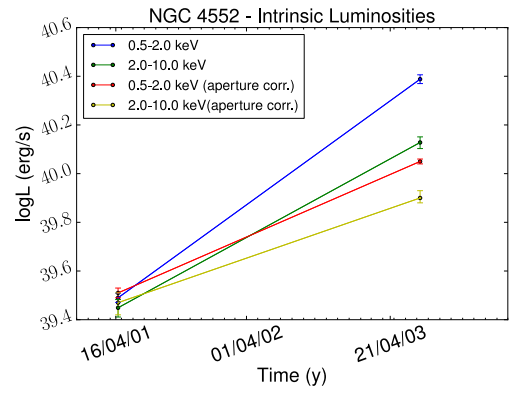
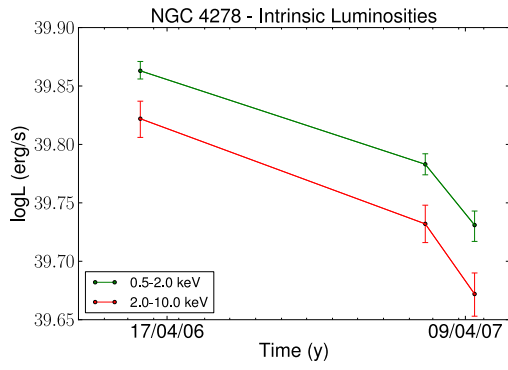


Table 2. Observational details. Instrument (Col. 1), obsID (Col. 2), date (Col. 3), aperture radius for the nuclear extraction (Col. 4), total exposure time (Col. 5), net exposure time (Col. 6), number of counts in the 0.5-10 keV band (Col. 7), hardness ratio (Col. 8)

, data from the optical monitor available (Col. 9).

NGC 1052								
Satellite	OBSID	Date	Radius	Exptime	Net Exptime	Counts	HR	OM
(1)	(2)	(3)	(4)	(5)	(6)	(7)	(8)	(9)
<i>XMM-Newton</i> ^c	093630101	2001-08-15	25	16.3	11.2	5818	0.28 _{-0.06} ^{+0.06}	No
<i>XMM-Newton</i>	306230101	2006-01-12	25	54.9	44.8	25565	0.34 _{-0.03} ^{+0.03}	Yes
<i>XMM-Newton</i>	553300301	2009-01-14	25	52.3	42.4	27367	0.39 _{-0.02} ^{+0.02}	Yes
<i>XMM-Newton</i> [*]	553300501	2009-01-14	25	8.0	5.4	320	-	No
<i>XMM-Newton</i>	553300401	2009-08-12	25	59.0	46.8	30643	0.42 _{-0.02} ^{+0.02}	Yes
<i>Chandra (ACIS-S)</i> [*]	385	2005-09-18	3	2.4	2.3	270	0.36 _{-0.24} ^{+0.24}	-
<i>Chandra (ACIS-S)</i> ^{*c}	5910	2000-08-29	3	60.0	59.2	6549	0.40 _{-0.04} ^{+0.04}	-
NGC 3226								
<i>XMM-Newton</i> ^c	0101040301	2000-11-28	15	40.1	30.2	6514	0.35 _{-0.04} ^{+0.04}	Yes
<i>XMM-Newton</i>	0400270101	2006-12-03	15	107.9	93.1	28199	-0.32 _{-0.01} ^{+0.01}	Yes
<i>Chandra (ACIS-S)</i> ^{*c}	860	1999-12-30	3	47.0	46.6	476	0.53 _{-0.12} ^{+0.12}	-
<i>Chandra (ACIS-S)</i> [*]	1616	2001-03-23	3	2.5	2.2	193	-0.20 _{-0.31} ^{+0.31}	-
NGC 3627								
<i>XMM-Newton</i> ^c	0093641101	2001-05-26	25	11.2	5.1	1181	-0.63 _{-0.02} ^{+0.02}	Yes
<i>Chandra (ACIS-S)</i> [*]	394	1999-11-03	8	1.8	1.8	7	-	-
<i>Chandra (ACIS-S)</i> ^c	9548	2008-03-31	8	50.2	49.5	964	-0.40 _{-0.05} ^{+0.05}	-
NGC 4261								
<i>Chandra (ACIS-S)</i>	834	2000-05-06	3	35.2	34.4	3465	-0.58 _{-0.01} ^{+0.01}	-
<i>Chandra (ACIS-S)</i> ^c	9569	2008-02-12	3	102.2	100.9	7757	-0.47 _{-0.01} ^{+0.01}	-
<i>XMM-Newton</i>	0056340101	2001-12-16	25	33.2	21.3	10730	-0.68 _{-0.01} ^{+0.01}	Yes
<i>XMM-Newton</i> ^c	0502120101	2007-12-16	25	127.0	63.0	32156	-0.68 _{-0.01} ^{+0.01}	Yes
NGC 4278								
<i>Chandra (ACIS-S)</i> [*]	398	2000-04-20	3	1.4	1.4	303	-0.55 _{-0.05} ^{+0.05}	-
<i>Chandra (ACIS-S)</i> [*]	4741	2005-02-03	3	37.9	37.5	20% pileup	-	-
<i>Chandra (ACIS-S)</i> ^c	7077	2006-03-16	3	111.7	110.3	9182	-0.66 _{-0.01} ^{+0.01}	-
<i>Chandra (ACIS-S)</i> [*]	7078	2006-07-25	3	52.1	51.4	18% pileup	-	-
<i>Chandra (ACIS-S)</i> [*]	7079	2006-10-24	3	106.4	105.1	16% pileup	-	-
<i>Chandra (ACIS-S)</i>	7081	2007-02-20	3	112.1	110.7	7591	-0.66 _{-0.01} ^{+0.01}	-
<i>Chandra (ACIS-S)</i>	7080	2007-04-20	3	56.5	55.8	3379	-0.69 _{-0.01} ^{+0.01}	-
<i>Chandra (ACIS-S)</i> [*]	11269	2010-03-15	3	83.0	81.9	2091	-0.82 _{-0.01} ^{+0.01}	-
<i>Chandra (ACIS-S)</i> [*]	12124	2010-03-20	3	26.2	25.8	576	-0.92 _{-0.01} ^{+0.01}	-
<i>XMM-Newton</i> ^{*c}	0205010101	2004-05-23	25	35.9	20.8	34516	-0.60 _{-0.01} ^{+0.01}	Yes
NGC 4552								
<i>Chandra (ACIS-S)</i> ^c	2072	2001-04-22	3	55.1	54.4	2288	-0.75 _{-0.01} ^{+0.01}	-
<i>XMM-Newton</i> ^c	0141570101	2003-07-10	25	44.8	17.3	12180	-0.81 _{-0.01} ^{+0.01}	Yes
NGC 5846								
<i>XMM-Newton</i> ^c	0021540101	2001-01-25	25	30.0	25.6	25905	-0.94 _{-0.01} ^{+0.01}	Yes
<i>XMM-Newton</i> ^d	0021540501	2001-08-26	25	19.7	10.0	10027	-0.95 _{-0.01} ^{+0.01}	Yes
<i>Chandra (ACIS-S)</i> ^c	788	2000-05-24	7	30.3	29.9	1839	-0.94 _{-0.01} ^{+0.01}	-
<i>Chandra (ACIS-I)</i>	7923	2007-06-12	7	91.2	90.0	2307	-0.88 _{-0.01} ^{+0.01}	-

* Observations were not used for the simultaneous fittings.

^c Observations used to compare *XMM-Newton* and *Chandra* data.^d Observation with only optical OM data (UV not available).

Table 3. F-test and $\chi^2/d.o.f$ applied to the SMF0. When no variation in one parameter is needed, we mark it as “-”. Name (Col. 1), instrument (Col. 2), best fit model (Col. 3), statistical test (Col. 4), parameter varying in respect to SMF0 (Col. 5, 6, 7, 8, 9 and 10) and the parameter that varies in SMF1 (Col. 11).

Name (1)	Instrument (2)	Best fit (3)	Test (4)	vs(N_{H1}) (5)	vs(N_{H2}) (6)	vs(kT) (7)	vs(Γ) (8)	vs($Norm_1$) (9)	vs($Norm_2$) (10)	Var. (11)
NGC 1052	<i>XMM</i>	ME2PL	F-test	1	2.29e-113	0.07	8.5071e-114	-	5.27e-128	$Norm_2$
			$\chi^2/d.o.f$	1.31	1.10	1.26	1.10	-	1.07	
NGC 3226	<i>XMM</i>	2PL	F-test	3.83e-158	1.3462e-194	-	0.09	2.58e-139	2.58e-139	N_{H2}
			$\chi^2/d.o.f$	1.18	0.98	-	2.57	1.30	1.30	
NGC 3627	<i>XMM/Ch</i>	MEPL	F-test	3.25e-20	8.24e-26	8.90e-10	0.05	2.17e-17	1.68e-25	N_{H2}
			$\chi^2/d.o.f$	2.27	1.63	4.21	6.54	2.76	1.71	
NGC 4261	<i>Chandra</i>	ME2PL	F-test	0.90	0.12	0.40	0.94	0.30	0.96	None
			$\chi^2/d.o.f$	1.27	1.26	1.26	1.27	1.26	1.27	
	<i>XMM</i>	ME2PL	F-test	0.09	0.39	0.34	0.92	-	0.75	None
			$\chi^2/d.o.f$	1.18	1.18	1.18	1.18	-	1.18	
NGC 4278	<i>Chandra</i>	MEPL	F-test	1.75e-07	1.03e-08	1.01e-07	4.94e-06	5.27e-18	6.73e-46	$Norm_2$
			$\chi^2/d.o.f$	1.53	1.51	1.53	1.56	1.36	1.00	
NGC 4552	<i>XMM/Ch</i>	MEPL	F-test	3.22e-128	4.13e-90	1.06e-53	1.45e-03	5.70e-133	6.76e-94	$Norm_1$
			$\chi^2/d.o.f$	4.01	6.82	11.35	22.7	3.75	6.47	
NGC 5846	<i>XMM</i>	MEPL	F-test	1	1	4.02e-04	0.38	0.05	0.66	None
			$\chi^2/d.o.f$	1.29	1.29	1.26	1.29	1.28	1.29	
	<i>Chandra</i>	MEPL	F-test	1	0.12	0.46	0.63	0.56	0.31	None
			$\chi^2/d.o.f$	0.97	0.95	0.97	0.97	0.97	0.96	

Table 4. F-test and $\chi^2/d.o.f$ applied to the SMF1. When no variation in one parameter is needed, we mark it as “-”. Name (Col. 1), instrument (Col. 2), the parameter varying in SMF1 (Col. 3), statistical test (Col. 4), parameter varying in respect to SMF1 (Col. 5, 6, 7, 8, 9 and 10) and the parameter that varies in SMF2 (Col. 11).

Name (1)	Instrument (2)	Var. (3)	Test (4)	vs(N_{H1}) (5)	vs(N_{H2}) (6)	vs(kT) (7)	vs(Γ) (8)	vs($Norm_1$) (9)	vs($Norm_2$) (10)	Var. (11)
NGC 1052	<i>XMM</i>	$Norm_2$	F-test	1	2.94e-10	0.03	4.12e-04	-	-	N_{H2}
			$\chi^2/d.o.f$	1.07	1.05	1.07	1.06	-	-	
NGC 3226	<i>XMM</i>	N_{H2}	F-test	1.59e-03	-	-	3.84e-07	1.75e-06	1.33e-06	None
			$\chi^2/d.o.f$	0.97	-	-	0.96	0.96	0.96	
NGC 3627	Both	N_{H2}	F-test	2.46e-03	-	0.35	0.01	1	2.92e-03	None
			$\chi^2/d.o.f$	1.46	-	1.63	1.52	2.44	1.47	
NGC 4278	<i>Chandra</i>	$Norm_2$	F-test	1	1	0.13	0.62	0.96	-	None
			$\chi^2/d.o.f$	1.00	1.00	0.99	1.00	1.00	-	
NGC 4552	Both	$Norm_1$	F-test	0.93	0.94	0.02	4.17e-10	-	4.15e-24	$Norm_2$
			$\chi^2/d.o.f$	1.65	1.65	1.62	1.50	-	1.28	

Table 5. Final compilation of the best fit models for the sample, including the individual best fit model for each observation, and the simultaneous best fit model with the varying parameters. Satellite (Col. 1), obsID (Col. 2), best fit model (Col. 3), parameters in the model (Col. 4, 5, 6, 7, 8 and 9) and $\chi^2/d.o.f$ (Col. 10).

Instrument	ObsID	Best fit	N_{H1} (10^{22} cm^{-2})	N_{H2} (10^{22} cm^{-2})	kT keV	Γ	$Norm_1$ (10^{-4})	$Norm_2$ (10^{-4})	$\chi^2/d.o.f$
(1)	(2)	(3)	(4)	(5)	(6)	(7)	(8)	(9)	(10)
NGC 1052									
XMM-Newton	093630101	ME2PL	-	13.77 ^{15.78} _{11.95}	0.62 ^{0.69} _{0.51}	1.24 ^{1.35} _{1.11}	1.05 ^{1.13} _{0.97}	6.09 ^{4.55} _{4.79}	269.16/234
XMM-Newton	306230101	ME2PL	-	9.30 ^{8.82} _{8.79}	0.50 ^{0.55} _{0.45}	1.30 ^{1.36} _{1.24}	1.05 ^{1.09} _{1.01}	7.20 ^{8.14} _{6.34}	799.19/822
XMM-Newton	553300301	ME2PL	-	8.96 ^{8.54} _{8.54}	0.61 ^{0.67} _{0.57}	1.38 ^{1.42} _{1.32}	1.09 ^{1.14} _{1.06}	10.16 ^{6.31} _{9.10}	923.38/869
XMM-Newton	553300401	ME2PL	-	9.47 ^{9.86} _{9.09}	0.53 ^{0.61} _{0.48}	1.43 ^{1.48} _{1.38}	1.10 ^{1.14} _{1.06}	12.02 ^{13.32} _{10.82}	1006.47/937
Chandra (3'')*	5910	ME2PL	-	5.33 ^{6.86} _{3.84}	0.64 ^{0.69} _{0.58}	1.21 ^{1.46} _{1.05}	0.37 ^{0.47} _{0.37}	0.57 ^{1.21} _{0.35}	261.04/226
Chandra (25'')*	5910	ME2PL	-	8.13 ^{11.49} _{5.36}	0.61 ^{0.65} _{0.57}	1.25 ^{1.50} _{1.00}	0.49 ^{0.66} _{0.49}	0.61 ^{1.21} _{0.19}	319.40/269
XMM-Newton	093630101	ME2PL	-	14.14 ^{15.77} _{12.66}	0.59 ^{0.61} _{0.57}	1.36 ^{1.39} _{1.33}	1.09 ^{1.11} _{1.06}	8.06 ^{8.89} _{7.31}	3043.69/2886
Simultaneous	306230101			9.80 ^{10.26} _{9.36}				8.38 ^{8.97} _{7.82}	
	553300301			8.75 ^{9.11} _{8.40}				9.74 ^{10.40} _{9.11}	
	553300401			9.21 ^{9.55} _{8.88}				10.41 ^{11.11} _{9.75}	
NGC 3226									
XMM-Newton	0101040301	2PL	0.11 ^{0.15} _{0.05}	1.03 ^{1.35} _{0.76}	-	1.69 ^{1.81} _{1.58}	0.71 ^{0.92} _{0.47}	1.85 ^{2.28} _{1.50}	245.87/252
XMM-Newton	0400270101	PL	0.17 ^{0.18} _{0.16}	-	-	1.74 ^{1.77} _{1.72}	-	-	635.19/663
Chandra (3'')*	860	PL	0.18 ^{0.00} _{0.00}	-	-	1.73 ^{1.10} _{1.07}	-	-	9.72/17
Chandra (25'')*	860	2PL	0.29 ^{0.70} _{0.10}	15.80 ^{114.58} _{0.00}	-	1.71 ^{3.00} _{1.34}	2.03 ^{4.48} _{0.00}	1.43 ^{16.49} _{0.00}	26.30/28
XMM-Newton	0101040301	2PL	0.09 ^{0.12} _{0.05}	0.86 ^{0.99} _{0.76}	-	1.73 ^{1.77} _{1.71}	0.86 ^{0.98} _{0.76}	1.89 ^{2.09} _{1.68}	905.42/920
Simultaneous	0400270101			0.22 ^{0.24} _{0.19}					
NGC 3627									
XMM-Newton	0093641101	MEPL	-	-	0.33 ^{0.52} _{0.29}	1.78 ^{2.09} _{1.57}	0.00 ^{0.02} _{0.00}	0.68 ^{0.83} _{0.60}	54.91/35
Chandra (8'')	9548	MEPL	-	0.05 ^{0.15} _{0.00}	0.65 ^{0.80} _{0.46}	1.45 ^{1.70} _{1.25}	0.06 ^{0.21} _{0.05}	0.24 ^{0.31} _{0.19}	33.63/34
Chandra (25'')*	9548	MEPL	-	-	0.40 ^{0.51} _{0.35}	1.49 ^{1.63} _{1.38}	0.31 ^{0.37} _{0.24}	0.55 ^{0.61} _{0.40}	149.42/96
Both	0093641101	MEPL	-	-	0.63 ^{0.68} _{0.58}	2.33 ^{2.42} _{2.25}	0.14 ^{0.15} _{0.12}	0.90 ^{0.96} _{0.85}	125.5/77
Simultaneous	9548			1.28 ^{1.48} _{1.11}					
NGC 4261									
Chandra	834	ME2PL	0.18 ^{0.47} _{0.49}	11.89 ^{16.01} _{9.31}	0.58 ^{0.60} _{0.58}	2.11 ^{3.07} _{1.52}	0.29 ^{0.55} _{0.37}	4.72 ^{25.76} _{14.97}	110.82/80
Chandra (3'')	9569	ME2PL	0.18 ^{0.08} _{0.08}	8.40 ^{10.20} _{6.90}	0.57 ^{0.56} _{0.56}	1.24 ^{1.31} _{1.07}	0.20 ^{0.20} _{0.20}	2.13 ^{1.18} _{1.18}	198.74/157
Chandra (25'')*	9569	ME2PL	-	9.03 ^{12.90} _{6.55}	0.61 ^{0.62} _{0.60}	1.16 ^{1.39} _{0.89}	0.35 ^{0.47} _{0.35}	0.64 ^{1.11} _{0.29}	382.42/218
Chandra	834/9569	ME2PL	0.18 ^{0.31} _{0.09}	9.38 ^{10.84} _{7.96}	0.57 ^{0.58} _{0.56}	1.87 ^{2.19} _{1.55}	0.27 ^{0.34} _{0.21}	2.70 ^{4.86} _{1.49}	312.57/247
Simultaneous									
XMM-Newton	0056340101	ME2PL	0.08 ^{0.15} _{0.01}	11.97 ^{14.73} _{9.31}	0.63 ^{0.64} _{0.61}	1.84 ^{2.22} _{1.45}	0.72 ^{0.94} _{0.54}	2.82 ^{6.30} _{1.11}	278.12/255
XMM-Newton	0502120101	ME2PL	0.04 ^{0.07} _{0.00}	9.71 ^{11.14} _{8.30}	0.64 ^{0.65} _{0.64}	1.75 ^{1.97} _{1.54}	0.64 ^{0.74} _{0.55}	2.30 ^{3.65} _{1.40}	563.80/461
XMM-Newton	0056340101	ME2PL	0.04 ^{0.08} _{0.01}	10.28 ^{11.56} _{9.02}	0.64 ^{0.65} _{0.63}	1.76 ^{1.95} _{1.57}	0.67 ^{0.76} _{0.58}	2.36 ^{3.54} _{1.53}	855.28/726
Simultaneous	0502120101								
NGC 4278									
Chandra(3'')	7077	MEPL	0.31 ^{0.58} _{0.05}	0.01 ^{0.03} _{0.00}	0.27 ^{0.38} _{0.19}	2.06 ^{2.15} _{1.99}	0.80 ^{0.21} _{0.18}	0.98 ^{1.06} _{0.90}	144.23/158
Chandra(25'')*	7077	MEPL	0.16 ^{0.45} _{0.01}	-	0.30 ^{0.37} _{0.21}	1.88 ^{1.95} _{1.83}	0.81 ^{1.36} _{0.77}	1.32 ^{1.39} _{1.27}	250.15/210
Chandra	7081	MEPL	-	-	0.63 ^{0.57} _{0.57}	2.03 ^{2.10} _{1.99}	0.13 ^{0.13} _{0.09}	0.77 ^{0.82} _{0.75}	155.54/145
Chandra	7080	MEPL	0.22 ^{0.71} _{0.00}	-	0.47 ^{0.61} _{0.18}	2.10 ^{2.25} _{2.03}	0.24 ^{13.76} _{0.07}	0.69 ^{0.79} _{0.65}	102.53/96
XMM-Newton*	0205010101	PL	0.02 ^{0.03} _{0.02}	-	-	2.04 ^{2.08} _{2.01}	-	-	562.25/529
Chandra	7077	MEPL	-	-	0.58 ^{0.62} _{0.48}	2.05 ^{2.11} _{2.03}	0.11 ^{0.12} _{0.10}	0.97 ^{1.02} _{0.82}	414.71/415
Simultaneous	7081							0.78 ^{0.77} _{0.65}	
	7080							0.68 ^{0.72} _{0.65}	
NGC 4552									
Chandra (3'')	2072	MEPL	0.23 ^{0.33} _{0.00}	-	0.65 ^{0.75} _{0.59}	1.85 ^{2.13} _{1.74}	0.36 ^{0.56} _{0.16}	0.29 ^{0.41} _{0.26}	72.49/67
Chandra (25'')*	2072	MEPL	0.03 ^{0.05} _{0.00}	0.00 ^{0.02} _{0.00}	0.60 ^{0.62} _{0.58}	1.89 ^{1.96} _{1.82}	1.64 ^{1.82} _{1.48}	0.91 ^{0.97} _{0.85}	161.64/133
XMM-Newton	0141570101	MEPL	0.01 ^{0.05} _{0.00}	-	0.59 ^{0.61} _{0.58}	1.92 ^{1.98} _{1.85}	2.12 ^{2.37} _{1.98}	1.46 ^{1.55} _{1.38}	282.04/254
Both	2072	MEPL	-	-	0.60 ^{0.62} _{0.59}	1.86 ^{1.91} _{1.81}	0.13 ^{0.17} _{0.13}	0.31 ^{0.33} _{0.29}	397.01/328
Simultaneous	0141570101						2.11 ^{2.33} _{1.96}	1.40 ^{1.48} _{1.32}	
NGC 5846									
XMM-Newton	0021540101	MEPL	-	-	0.61 ^{0.61} _{0.60}	2.05 ^{2.17} _{1.92}	5.09 ^{5.17} _{5.00}	0.61 ^{0.68} _{0.53}	356.05/266
XMM-Newton	0021540501	MEPL	0.04 ^{0.07} _{0.01}	-	0.62 ^{0.63} _{0.60}	2.20 ^{2.40} _{2.14}	5.55 ^{6.07} _{5.10}	0.69 ^{0.81} _{0.56}	227.57/194
XMM-Newton	0021540101	MEPL	-	-	0.62 ^{0.62} _{0.61}	2.05 ^{2.14} _{1.94}	5.06 ^{5.10} _{4.98}	0.61 ^{0.67} _{0.54}	606.06/469
Simultaneous	0021540501								
Chandra(7'')	788	MEPL	-	0.21 ^{0.43} _{0.00}	0.61 ^{0.64} _{0.57}	3.06 ^{3.24} _{2.24}	0.52 ^{0.79} _{0.48}	0.40 ^{0.76} _{0.18}	41.72/50
Chandra(25'')*	788	MEPL	-	-	0.62 ^{0.63} _{0.60}	1.53 ^{1.99} _{1.27}	2.83 ^{3.97} _{2.13}	0.67 ^{0.81} _{0.53}	188.51/137
Chandra	7923	MEPL	0.11 ^{0.18} _{0.00}	0.08 ^{0.33} _{0.00}	0.60 ^{0.62} _{0.57}	2.73 ^{3.20} _{2.27}	0.77 ^{0.98} _{0.54}	0.21 ^{0.38} _{0.12}	63.24/59
Chandra	788/7923	MEPL	-	0.21 ^{0.38} _{0.14}	0.62 ^{0.64} _{0.60}	3.11 ^{3.40} _{2.40}	0.52 ^{0.56} _{0.48}	0.38 ^{0.68} _{0.23}	105.82/110
Simultaneous									

* Observations not used in the simultaneous fit.

Table 6. Soft (0.5-2 keV) and hard (2-10 keV) intrinsic luminosities for individual (Col. 3 and 5) and simultaneous (Col. 4 and 6) fitting.

NGC 1052						
Satellite	ObsID	log(L(0.5-2 keV)) Individual	log(L(0.5-2 keV)) Simultaneous	log(L(2-10 keV)) Individual	log(L(2-10 keV)) Simultaneous	
(1)	(2)	(3)	(4)	(5)	(6)	
<i>XMM-Newton</i>	093630101	40.955 [40.941 - 40.969]	40.992 [40.987 - 40.996]	41.460 [41.447 - 41.473]	41.473 [41.458 - 41.488]	
<i>XMM-Newton</i>	306230101	40.960 [40.953 - 40.967]	41.006 [41.002 - 41.011]	41.483 [41.477 - 41.489]	41.488 [41.481 - 41.494]	
<i>XMM-Newton</i>	553300301	41.104 [41.096 - 41.112]	41.063 [41.058 - 41.068]	41.555 [41.549 - 41.561]	41.545 [41.539 - 41.551]	
<i>XMM-Newton</i>	553300401	41.117 [41.110 - 41.125]	41.089 [41.084 - 41.093]	41.551 [41.545 - 41.556]	41.571 [41.565 - 41.577]	
<i>Chandra</i> (3'')	5910	40.186 [40.169 - 40.202]	-	41.290 [41.266 - 41.292]	-	
<i>Chandra</i> (25'')	5910	40.290 [40.274 - 40.306]	-	41.336 [41.299 - 41.370]	-	
NGC 3226						
<i>XMM-Newton</i>	0101040301	40.762 [40.750 - 40.774]	40.775 [40.763 - 40.786]	41.057 [41.041 - 41.072]	41.013 [41.004 - 41.021]	
<i>XMM-Newton</i>	0400270101	40.782 [40.777 - 40.787]	40.775 [40.769 - 40.780]	40.994 [40.986 - 41.003]	41.013 [41.005 - 41.021]	
<i>Chandra</i> (3'')	860	40.473 [40.378 - 40.552]	-	40.685 [- 41.311]	-	
<i>Chandra</i> (25'')	860	40.552[40.495 - 40.602]	-	40.909[- 41.313]	-	
NGC 3627						
<i>XMM-Newton</i>	0093641101	39.440 [39.417 - 39.462]	39.452 [39.429 - 39.474]	39.420 [39.362 - 39.472]	39.245 [39.197 - 39.288]	
<i>Chandra</i> (8'')	9548	38.900 [38.854 - 38.942]	39.452 [39.421 - 39.481]	39.169 [- 41.072]	39.224 [39.179 - 39.264]	
<i>Chandra</i> (25'')	9548	39.367 [39.348 - 39.386]	-	39.536 [39.268 - 39.701]	-	
NGC 4261						
<i>Chandra</i>	834	41.180 [41.161 - 41.197]	40.976 [40.967 - 40.984]	41.107 [40.857 - 41.265]	41.018 [40.971 - 41.060]	
<i>Chandra</i> (3'')	9569	40.924 [40.913 - 40.935]	40.976 [40.967 - 40.984]	40.996 [41.084 - 40.887]	41.018 [40.971 - 41.060]	
<i>Chandra</i> (25'')	9569	40.794 [40.779 - 40.807]	-	40.967 [40.940 - 40.993]	-	
<i>XMM-Newton</i>	0056340101	41.301 [41.293 - 41.309]	41.142 [41.138 - 41.146]	41.188 [41.166 - 41.209]	41.132 [41.113 - 41.151]	
<i>XMM-Newton</i>	0502120101	41.223 [41.219 - 41.227]	41.142 [41.138 - 41.146]	41.148 [41.136 - 41.160]	41.132 [41.113 - 41.151]	
NGC 4278						
<i>Chandra</i> (3'')	7077	39.873 [39.865 - 39.881]	39.863 [39.856 - 39.871]	39.762 [39.319 - 39.977]	39.822 [39.806 - 39.837]	
<i>Chandra</i> (25'')	7077	40.137 [40.102 - 40.169]	-	40.061 [40.035 - 40.084]	-	
<i>Chandra</i>	7081	39.314 [39.303 - 39.324]	39.783 [39.774 - 39.792]	39.269 [39.244 - 39.293]	39.732 [39.716 - 39.748]	
<i>Chandra</i>	7080	39.778 [39.741 - 39.813]	39.731 [39.717 - 39.743]	39.615 [- 40.728]	39.672 [39.653 - 39.690]	
<i>XMM-Newton</i>	0205010101	40.733 [40.729 - 40.736]	-	40.768 [40.759 - 40.777]	-	
NGC 4552						
<i>Chandra</i> (3'')	2072	39.687 [39.625 - 39.742]	39.490 [39.471 - 39.509]	39.463 [39.045 - 40.147]	39.449 [39.411 - 39.483]	
<i>Chandra</i> (25'')	2072	40.252 [40.239 - 40.266]	-	39.904 [39.819 - 39.974]	-	
<i>XMM-Newton</i>	0141570101	40.396 [40.389 - 40.403]	40.388 [40.370 - 40.406]	40.128 [40.103 - 40.151]	40.128 [40.103 - 40.151]	
NGC 5846						
<i>XMM-Newton</i>	0021540101	41.083 [41.079 - 41.088]	41.080 [41.076 - 41.084]	40.196 [40.163 - 40.227]	40.189 [40.160 - 40.216]	
<i>XMM-Newton</i>	0021540501	41.122 [41.114 - 41.130]	41.080 [41.076 - 41.084]	40.165 [40.115 - 40.210]	40.189 [40.160 - 40.216]	
<i>Chandra</i> (7'')	788	40.159 [40.118 - 40.195]	40.291 [40.244 - 40.334]	38.586 [38.528 - 38.637]	39.326 [39.067 - 39.486]	
<i>Chandra</i> (25'')	788	40.867 [40.853 - 40.880]	-	40.552 [40.407 - 40.661]	-	
<i>Chandra</i>	7923	40.490 [40.471 - 40.507]	40.291 [40.244 - 40.334]	38.809 [38.760 - 38.853]	39.326 [39.067 - 39.486]	

Table 7. Results for the best fit of the annular region (ring) in *Chandra* data, and the best fit obtained for the nucleus of *XMM-Newton* data when the contribution from the annular region was removed. Name and obsID in parenthesis (Col. 1), extracted region (Col. 2), best fit model (Col. 3), parameters of the best fit model (Col. 4, 5, 6, 7 and 8), soft and hard intrinsic luminosities (Col. 9 and 10), and the percentage of the contribution from the ring to the 25'' aperture *Chandra* data in the 0.5-10.0 keV band (Col. 11).

Name (obsID)	Region	Model	N_{H1} (10^{22}cm^{-2})	N_{H2} (10^{22}cm^{-2})	kT (keV)	Γ	χ_r^2	$\log L_{\text{soft}}$ (0.5-2 keV)	$\log L_{\text{hard}}$ (2-10 keV)	Cont. %
(1)	(2)	(3)	(4)	(5)	(6)	(7)	(8)	(9)	(10)	(11)
NGC 1052 (5910)	Ring	ME2PL	-	$26.10^{38.14}_{16.93}$	$0.31^{0.39}_{0.28}$	$1.98^{2.23}_{1.71}$	1.47	40.185	40.563	10
NGC 1052 (093630101)	Nucleus	ME2PL	-	$7.54^{9.98}_{5.20}$	$0.78^{0.89}_{0.68}$	$1.69^{1.86}_{1.50}$	1.13	39.875	41.235	
NGC 3226 (860)	Ring	PL	-	-	-	$1.42^{1.07}_{1.85}$	1.89	40.482	40.557	20
NGC 3226 (0101040301)	Nucleus	2PL	$0.35^{1.88}_{0.00}$	$1.02^{1.88}_{0.00}$	-	$1.72^{1.88}_{1.58}$	1.00	40.623	40.912	
NGC 3627 (9548)	Ring	MEPL	-	-	$0.41^{0.49}_{0.35}$	$1.71^{1.85}_{1.58}$	1.35	39.302	39.384	92
NGC 3627 (093641101)	Nucleus	MEPL	-	-	$0.71^{1.02}_{0.40}$	$3.37^{3.76}_{2.97}$	1.16	38.990	38.125	
NGC 4261 (9569)	Ring	MEPL	$0.06^{0.11}_{0.03}$	$0.00^{0.04}_{0.00}$	$0.61^{0.62}_{0.59}$	$1.87^{2.07}_{1.70}$	2.07	40.663	40.252	37
NGC 4261 (0502120101)	Nucleus	ME2PL	-	$8.29^{9.89}_{7.28}$	$0.67^{0.68}_{0.65}$	$1.56^{1.72}_{1.41}$	1.21	40.857	41.051	
NGC 4278 (7077)	Ring	MEPL	-	-	$0.29^{0.36}_{0.19}$	$1.61^{1.71}_{1.51}$	1.12	39.551	39.707	38
NGC 4278 (0205010101)	Nucleus	PL	$0.02^{0.03}_{0.02}$	-	-	$2.05^{2.10}_{2.03}$	1.05	40.681	40.736	
NGC 4552 (2072)	Ring	MEPL	-	-	$0.60^{0.62}_{0.57}$	$1.92^{2.06}_{1.81}$	1.47	39.648	39.304	23
NGC 4552 (0141570101)	Nucleus	MEPL	-	-	$0.58^{0.62}_{0.52}$	$1.90^{2.06}_{1.80}$	1.10	40.053	39.878	
NGC 5846 (788)	Ring	MEPL	-	-	$0.61^{0.62}_{0.59}$	$1.87^{2.46}_{1.61}$	1.63	40.815	40.217	73
NGC 5846 (0021540101)	Nucleus	MEPL	-	-	$0.63^{0.64}_{0.61}$	$4.00^{3.56}_{3.56}$	1.36	40.753	39.171	

Table 8. Simultaneous fittings taking into account the contribution from the annular region given in Table 7. Name and obsID in parenthesis (Col. 1), parameters of the best fit model (Col. 2, 3, 4, 5, 6 and 7), $\chi^2/d.o.f$ (Col. 8) and soft and hard intrinsic luminosities (Col. 9 and 10).

ObsID	N_{H1} (10^{22}cm^{-2})	N_{H2} (10^{22}cm^{-2})	kT (keV)	Γ	$Norm_1$ (10^{-4})	$Norm_2$ (10^{-4})	$\chi^2/d.o.f$	$\log L_{\text{soft}}$ (0.5-2 keV)	$\log L_{\text{hard}}$ (2-10 keV)
(1)	(2)	(3)	(4)	(5)	(6)	(7)	(8)	(9)	(10)
NGC 1052									
0093630101	-	$6.11^{7.18}_{5.07}$	$0.68^{0.73}_{0.63}$	$1.58^{1.70}_{1.47}$	$0.48^{0.53}_{0.44}$	$1.28^{1.69}_{0.95}$	577.98/477	$40.35^{40.36}_{40.34}$	$41.33^{41.35}_{41.32}$
5910								$40.35^{40.36}_{40.34}$	$41.27^{41.28}_{41.26}$
NGC 3226									
0101040301	$0.34^{0.01}_{0.54}$	$1.03^{1.42}_{0.68}$	-	$1.72^{1.86}_{1.60}$	$0.55^{0.93}_{0.03}$	$1.59^{2.23}_{2.11}$	268.434/279	$40.710^{40.732}_{40.688}$	$41.681^{41.725}_{41.633}$
860		$0.07^{0.00}_{0.32}$				$0.68^{0.92}_{0.34}$		$40.510^{40.581}_{40.425}$	$40.958^{40.978}_{40.938}$
NGC 4261									
0502120101	$0.03^{0.08}_{0.00}$	$7.64^{8.74}_{6.58}$	$0.60^{0.61}_{0.59}$	$1.55^{1.75}_{1.36}$	$0.22^{0.26}_{0.19}$	$1.53^{2.25}_{1.04}$	972.83/627	$40.84^{40.84}_{40.83}$	$41.03^{41.05}_{41.01}$
9569								$40.84^{40.85}_{40.83}$	$40.99^{41.01}_{40.97}$
NGC 4278									
0205010101	$0.03^{0.03}_{0.02}$	-	-	$2.11^{2.14}_{2.08}$	$7.74^{7.95}_{7.54}$		844.93/690	$40.71^{40.72}_{40.71}$	$40.71^{40.72}_{40.70}$
7077					$1.15^{1.18}_{1.11}$			$39.89^{39.89}_{39.88}$	$39.86^{39.87}_{39.84}$
NGC 4552									
0141570101	$0.02^{0.04}_{0.00}$	$0.01^{0.05}_{0.00}$	$0.64^{0.66}_{0.61}$	$1.85^{2.00}_{1.78}$	$0.77^{0.90}_{0.70}$	$0.84^{1.01}_{0.76}$	380.50/327	$40.05^{40.05}_{40.04}$	$39.90^{39.93}_{39.88}$
2072					$0.16^{0.18}_{0.14}$	$0.31^{0.37}_{0.28}$		$39.51^{39.53}_{39.49}$	$39.47^{39.51}_{39.42}$

Table 9. Statistics for the light curves. Name (Col. 1), obsID (Col. 2), $\chi^2/d.o.f$ and the probability of being variable (Col. 3 and 4) and normalized excess variance with errors (Col. 5 and 6).

Name	ObsID	$\chi^2/d.o.f$	Prob. (%)	σ^2 (10^{-2})	$err(\sigma^2)$ (10^{-2})
(1)	(2)	(3)	(4)	(5)	(6)
NGC 1052	0093630101	18.6/11	93	0.189	0.107
	0306230101	57.1/49	80	0.043	0.046
	0553300301	49.5/46	66	0.022	0.043
	0553300401	39.3/49	16	-0.042	0.042
	5910	48.6/59	17	-0.157	0.173
NGC 3226	860	51.2/45	76	-0.047	0.028
	0101040301	35.0/32	67	0.074	0.195
	0400270101	474.1/100	100	1.781	0.079
NGC 3627	0093641101	2.6/5	24	-0.312	0.605
	9548	63.8/49	92	0.360	0.351
NGC 4261	834	35.8/34	62	0.077	0.267
	9569	85.7/100	15	-0.243	0.195
	0056340101	25.4/19	85	0.109	0.099
	0502120101	79.6/64	91	0.075	0.057
NGC 4278	7077	124.3/111	82	0.149	0.184
	7081	91.4/107	14	-0.299	0.227
	7080	41.0/55	8	-0.445	0.354
	0205010101	2.2/11	0	-0.074	0.041
NGC 4552	2072	57.4/45	90	0.089	0.570
	0141570101	12.8/14	46	0.000	0.081
NGC 5846	0021540101	20.1/28	14	-0.034	0.037
	0021540501	7.9/8	56	0.014	0.070
	788	20.4/16	80	0.513	0.640
	7923	85.2/86	50	-0.136	0.560

Table 10. UV luminosities derived from the OM observations. Name (Col. 1), obsID (Col. 2), filter (Col. 3) and luminosity (Col. 4).

Name	ObsID	Filter	logL (erg/s)	α_{ox}
(1)	(2)	(3)	(4)	(5)
NGC 1052	0306230101	UVM2	41.038 \pm 0.013	-0.94 \pm 0.03
	0306230101	UVW2	40.938 \pm 0.028	
	0553300301	UVM2	41.139 \pm 0.012	-0.95 \pm 0.03
	0553300301	UVW2	40.947 \pm 0.026	
	0553300401	UVM2	41.041 \pm 0.014	-0.91 \pm 0.03
NGC 3226	0553300401	UVW2	40.885 \pm 0.025	
	0101040301	UVW1	41.375 \pm 0.006	-1.15 \pm 0.70
	0400270101	UVW1	41.327 \pm 0.001	*
NGC 3627	0093641101	UVW1	41.367 \pm 0.007	-1.66 \pm 0.05
NGC 4261	0056340101	UVM2	41.431 \pm 0.024	-1.04 \pm 0.05
	0056340101	UVW1	42.169 \pm 0.005	
	0502120201	UVM2	41.609 \pm 0.014	-1.11 \pm 0.03
NGC 4278	0502120201	UVW1	42.214 \pm 0.001	
	0205010101	UVW1	40.903 \pm 0.020	-1.11 \pm 0.02
NGC 4552	0141570101	UVW2	41.273 \pm 0.033	-1.28 \pm 0.04
NGC 5846	0021540101	UVW2	40.561 \pm 0.148	-0.81 \pm 0.14

* The observation was not used (see text).

Table 11. Summary. Name, and the instrument in parenthesis (Col. 1), type (Col. 2), logarithm of the soft (0.5-2 keV) and hard (2-10 keV) X-ray luminosities, where the mean was calculated or *Chandra* luminosity was given when both instruments were used, and percentages in flux variations (Col. 3 and 4), black hole mass in logarithmical scale, from González-Martín et al. (2009a) (Col. 5), Eddington ratio, calculated from Eracleous et al. (2010a) using $L_{bol} = 33L_{2-10keV}$ (Col. 6), best-fit for the SMF0 (Col. 7), parameter varying in SMF1, with the percentage of variation (Col. 8), parameter varying in SMF2, with the percentage of variation (Col. 9), the sampling time-scale for variations (Col. 10), and variations in the hardness ratios (Col. 11).

Name	Type	$\log L_{soft}$ (0.5-2 keV)	$\log L_{hard}$ (2-10 keV)	$\log M_{BH}$	L_{bol}/L_{Edd}	SMF0	Variability SMF1	SMF2	T (Years)	HR
(1)	(2)	(3)	(4)	(5)	(6)	(7)	(8)	(9)	(10)	(11)
NGC 1052 (X)	AGN	41.04	41.52	8.07	7.2×10^{-4}	ME2PL	$Norm_2$ 49%	N_{H2} 31%	8	33%
	1.9	20%	20%							
NGC 3226 (X,C)	AGN	40.78	41.01	8.22	1.6×10^{-4}	2PL	N_{H2} 93%	$Norm_2$ 57%	1	
	1.9	37%	81%							
NGC 4261 (X)	AGN	40.98	41.02	8.96	2.9×10^{-5}	ME2PL	-	-	8	0%
	2	0%	0%							
(C)						ME2PL	-	-	6	19%
		0%	0%							
NGC 4278 (C)	AGN	39.80	39.75	8.46	5.0×10^{-6}	MEPL	$Norm_2$ 30%	-	1	40%*
	1.9	26%	29%							
NGC 4552 (X,C)	AGN	39.49	39.45	8.84	1.0×10^{-6}	MEPL	$Norm_1$ 93%	$Norm_2$ 78%	2	
	2	73%	63%							
NGC 5846 (X)	Non-AGN	40.29	39.33	8.49	1.8×10^{-6}	MEPL	-	-	7	1%
	2	0%	0%							
(C)						MEPL	-	-	0.6	6%
		0%	0%							

* For all *Chandra* data. With useful spectroscopic data variations are 4% .

Fig. 3. Anticorrelation between the spectral index, Γ from individual fits, vs. the Eddington ratio, $\log(L_{bol}/L_{Edd})$, for our sample galaxies. The solid line represents the relation given by Younes et al. (2011), while the dashed line represents that by (Gu & Cao 2009), both shifted to the same bolometric correction (see text).

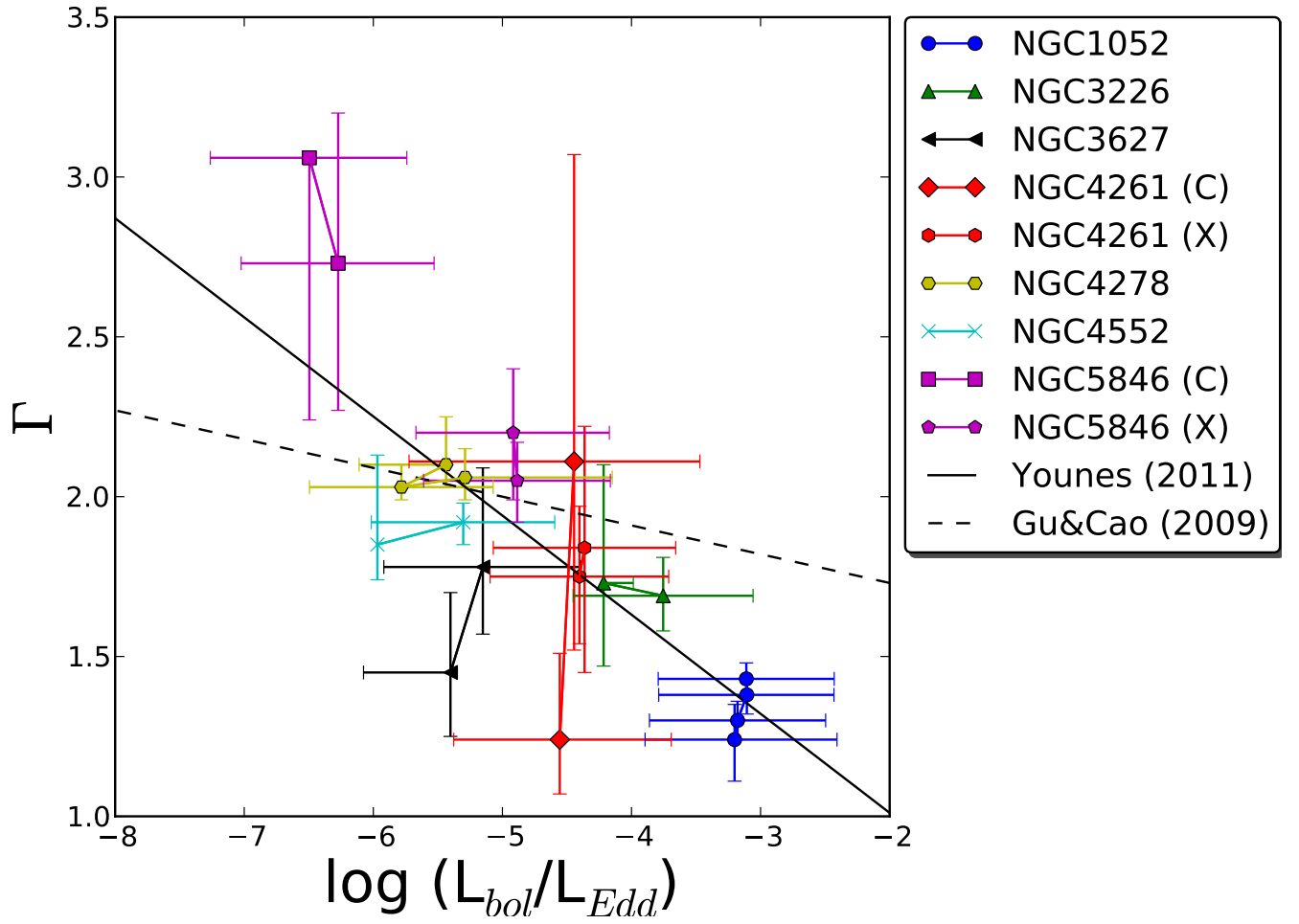
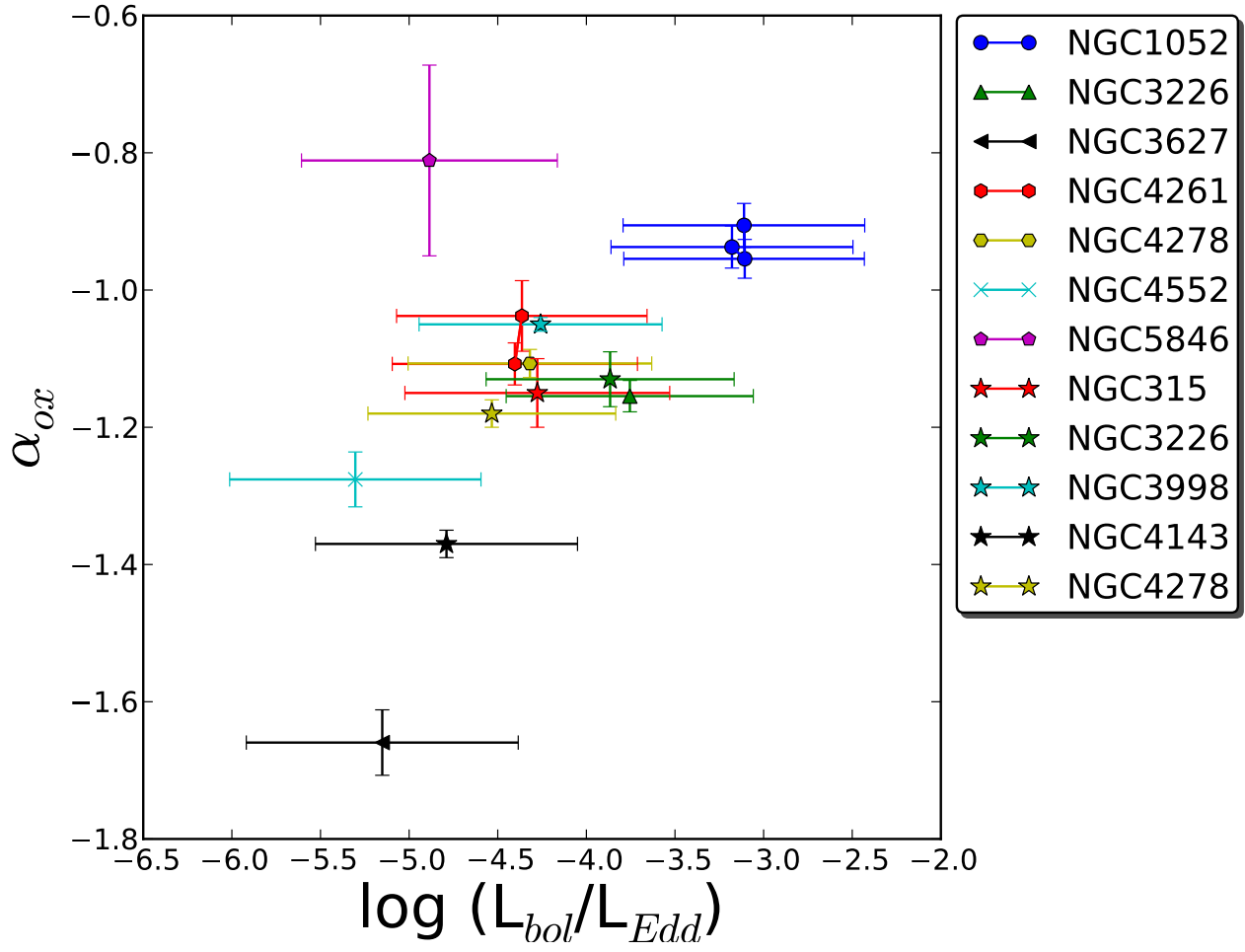


Fig. 4. Correlation between the spectral index, α_{ox} , vs. the Eddington ratio, $\log(L_{bol}/L_{Edd})$. Starred symbols correspond to the sources in Younes et al. (2012).



Appendix A: Notes and comparisons with previous results for individual objects

A.1. NGC 1052

The brightest elliptical galaxy in the Cetus I group, NGC 1052, already classed as a LINER in the pioneering work by Heckman (1980), was classified as LINER type 1.9 by Ho et al. (1997).

NGC 1052 was observed twice with *Chandra* and five times with the *XMM-Newton* satellite, what makes it a good candidate for studying variability. The general characteristics of the two *Chandra* observations ObsID 385 (taken in 2000) and ObsID 5910 (2005) were reported by González-Martín et al. (2009b) and Boroson et al. (2011), respectively, showing quite different spectral behaviour with a flatter spectral index, lower N_H and lower luminosity in 2005. We analyzed the observation from 2005 and found a different spectral fit from Boroson et al. (2011), since they used a PL model to fit the spectrum. However, similar luminosities were found between González-Martín et al. (2009b), Boroson et al. (2011) and this work (with $\log(L(2-10 \text{ keV}))=41.4^{+0.1}_{-0.8}$, $41.4^{+0.01}_{-0.01}$ and $41.3^{+0.00}_{-0.02}$, respectively).

Only one *XMM-Newton* observation (ObsID 306230101 taken in 2006) was previously analyzed by González-Martín et al. (2009b) and Brightman & Nandra (2011), showing quite similar results, with Brightman & Nandra (2011) in spite of a more absorbed spectrum in the latter. Our results are in good agreement with those provided by González-Martín et al. (2009b). The most recent observation at X-rays reported so far is a 100 ks observation taken with *SUZAKU* in 2007. The derived spectral characteristics reported by Brenneman et al. (2009) appear to be similar to those from *XMM-Newton* which is compatible with the values in González-Martín et al. (2009b), Brightman & Nandra (2011) and this paper (intrinsic luminosity of $\log(L(2-10 \text{ keV})) \sim 41.5$).

In the UV range, Maoz et al. (2005) studied this galaxy with *HST* ACS and found a decrease in the flux of the source of a factor of 2 between the 1997 data reported by Pogge et al. (2000) and their 2002 dataset. We found UV flux variations of a factor of 1.3 from *XMM-OM* data in seven months.

A.2. NGC 3226

NGC 3226 is a dwarf elliptical galaxy, which is strongly interacting with the Seyfert 1.5 galaxy NGC 3227, located at $2'$ in projected distance (see Figure C.19 in González-Martín et al. 2009b). NGC 3226 was classified by Ho et al. (1997) as a type 1.9 LINER.

This galaxy was observed two times with *Chandra*-ACIS in 1999 and 2001 and four times with *XMM-Newton* from 2000 to 2006.

Chandra data taken in 1999 were analyzed by George et al. (2001) and those taken in 2001 by Terashima & Wilson (2003). In both cases the X-ray spectra were fitted to a single power law, but with differing column densities, the data in 2001 being a factor 2 more absorbed; this leads to a difference in the X-ray luminosity in the hard (2-10 keV) band of 70%. The reanalysis of these data performed by Younes et al. (2011) shows spectral parameters consistent with the previous studies although their estimated difference in luminosity is lower (40%). We did not use these data because obsID 1616 does not match our criteria of the minimum number of counts.

The analysis by Gondoin et al. (2004) of snapshot *XMM-Newton* observations taken in 2000 also showed an X-ray spectrum consistent with a power law with $\log(L(2-10 \text{ keV})) = 40.38^{+0.01}$, close to the value obtained by George et al. (2001), $\log(L(2-10 \text{ keV})) = 40.26^{+0.01}$, for the same epoch. Binder et al. (2009) studied the *XMM-Newton* observation from 2006 and found significant short time scale flux variation, with a fractional variability amplitude of 11.7. They compare their measurements, $\log(L(0.4-2 \text{ keV})) = 40.47^{+0.01}_{-0.00}$ and $\log(L(2-10 \text{ keV})) = 40.55^{+0.02}_{-0.08}$, with those from Gondoin et al. (2004) (see above), finding variability on time-scales of years. Younes et al. (2011) analyzed the longest exposure data from 2000 and 2006 and found a difference in the hard luminosity of 40%. Considering both, *Chandra* and *XMM-Newton* data (obsID. 860 and 1616, 0101040301 and 0400270101, respectively), they concluded that the source variability is due to modifications in the N_H . We find spectral parameters in agreement to what Younes et al. (2011) found for the *XMM-Newton* and *Chandra* data, and we obtained a $\chi_r^2 = 4.7$ for obsID 0400270101, but this observation seemed to be affected by the presence of the rapid variable Seyfert 1.5 NGC 3227. Binder et al. (2009) and Younes et al. (2011) found similar results for this galaxy, interpretation of such variability was related to outflows or feedback processes.

A.3. NGC 3627

Together with NGC 3628 and NGC 3623, these three galaxies form the Leo Triplet (see Figure C.27 in González-Martín et al. (2009b)). Cappellari et al. (1999) classified it as type 2.0 LINER.

This galaxy was observed twice with *Chandra*, in 1999 and 2008, and once with *XMM-Newton*, in 2001.

Ho et al. (2001) and Panessa et al. (2006) studied *Chandra* ObsID 394 from 1999, using a PL model with $\Gamma = 1.8$, deriving similar luminosities, $\log(L(2-10 \text{ keV})) = 37.6$ and 37.9 , respectively. *Chandra* ObsID 9548 was analyzed by Grier et al. (2011), who used a PL with $\Gamma = 2$ to get $\log(L(0.3-8 \text{ keV})) = 38.51 \pm 0.03$. We used a MEPL model to fit this spectrum and obtained greater luminosity $\log(L(2-10 \text{ keV})) = 39.2^{+1.9}$, the difference most probably due to the different models used for the analysis. The *XMM-Newton* observation was analyzed by González-Martín et al. (2009b) and Brightman & Nandra (2011) who used PL and MEPL models to calculate luminosities, and derived $\log(L(2-10 \text{ keV})) = 39.2 \pm 0.1$ and 39.5 , respectively, with which our results agree (39.4 ± 0.1).

No information on UV was found in the literature.

A.4. NGC 4261

NGC 4261 contains a pair of symmetric kpc-scale jets (Birkinshaw & Davies 1985) and a nuclear disc of dust roughly perpendicular to the radio jet (Ferrarese et al. 1996). Ho et al. (1997) classified it as type 2.0 LINER.

It has been observed twice with *Chandra*, in 2000 and 2008, and with *XMM-Newton* in other three epochs from 2001 to 2007. However, only the analyses on *Chandra* ObsID 834 and *XMM-Newton* ObsID 56340101 are published.

Satyapal et al. (2005), Rinn et al. (2005) and Donato et al. (2004) reported quite consistent spectral parameters by fitting the *Chandra* spectra with a thermal and a power law component but with a range of variation in the reported luminosities $\log(L(2-10 \text{ keV}))$ between 40.5 and 41.0. On the other side González-Martín et al. (2009b) and Zezas et al. (2005) fitted the spectra with a ME2PL, using the same value for the spectral index for the two PL in the case of González-Martín et al. (2009b) and varying the spectral index in the case of Zezas et al. (2005). The comparison of the spectral parameters is quite consistent with the largest difference being the N_{H} , $16.45 \times 10^{22} \text{ cm}^{-2}$ for González-Martín et al. (2009b) and $8.4 \times 10^{22} \text{ cm}^{-2}$ for Zezas et al. (2005); this leads to a higher luminosity in Zezas et al. (2005), $\log(L(2-10 \text{ keV})) = 42.0$, against $\log(L(2-10 \text{ keV})) = 41.1^{+0.1}_{-0.7}$ in González-Martín et al. (2009b). We used the ME2PL model to fit this spectrum and found spectral parameters and luminosities in agreement with González-Martín et al. (2009b).

The *XMM-Newton* observation ObsID 056340101 taken in 2001 was analyzed by González-Martín et al. (2009b), Sambruna et al. (2003) and Gliozzi et al. (2003). Different models were used for the three works: an absorbed PL (Gliozzi et al. 2003), an absorbed MEPL (Sambruna et al. 2003) and a ME2PL (González-Martín et al. 2009b). This could explain, in principle, the different luminosities reported. Our results ($\log L(2-10 \text{ keV}) = 41.13 \pm 0.02$) are in good agreement with the spectral parameters and luminosities ($41.2^{+0.0}_{-0.7}$) reported by González-Martín et al. (2009b), but not with those obtained by Sambruna et al. (2003) and Gliozzi et al. (2003) (41.9).

Information from the UV was not found in the literature.

A.5. NGC 4278

NGC 4278 is an elliptical galaxy classified as type 1.9 LINER by Ho et al. (1997), who found a relatively weak, broad H_{α} line. The north-northwest side of the galaxy is heavily obscured by large-scale dust-lanes, whose distribution shows several dense knots interconnected by filaments (Carollo et al. 1997).

This galaxy has been observed in nine occasions with *Chandra* from 2000 to 2010 and once with *XMM-Newton* in 2004. Brassington et al. (2009) used six *Chandra* observations and found 97 variable sources within NGC 4278, in an elliptical area of $4'$ centered in the nucleus. None of them are within the aperture of $3''$ we used for the nuclear extraction. *Chandra* observations were taken by G. Fabbiano to study the plethora of sources detected in this galaxy (~ 250) (see Brassington et al. (2009) and Boroson et al. (2011)). The nuclear source was studied by González-Martín et al. (2009b) using *Chandra* obsID 7077 taken in 2006 and *XMM-Newton* data. They found a hard X-ray luminosity difference of a factor of 10 between the two observations, that were attributed to the contamination of the numerous sources around the nucleus.

The nuclear variability of this source has been already studied by Younes et al. (2010). They conclude that long time-scale

(months) variability is detected with a flux increase of a factor of ~ 3 on a time-scale of a few months and a factor of 5 between the faintest and the brightest observation separated by ~ 3 years. We used three of these observations, our spectral fittings being in good agreement with theirs, although we found smaller variations in luminosities. Whereas the different *Chandra* observations did not show short time-scale (minutes to hours) variability, during the *XMM-Newton* observation, where the highest flux level was detected, they found a 10% flux increase on a short time-scale of a few hours. With the same dataset we got a 3% variation in the same time range, the difference being most probably due to the different apertures used for the analysis.

In the UV, Cardullo et al. (2008) found that the luminosity increased a factor of 1.6 in around six months using data from *HST* WFPC2/F218W.

A.6. NGC 4552

This Virgo elliptical galaxy has been classified as LINER 2.0 (Cappellari et al. 1999). A radio jet was detected with *VLBI* observations (Nagar et al. 2005).

It has been observed four times with *Chandra* from 2001 to 2012 and with *XMM-Newton* in a single epoch in 2003. However, three of the *Chandra* observations are not public yet, so the only reported results came from *Chandra* ObsID 2072 (Filho et al. 2004; Xu et al. 2005; González-Martín et al. 2009b; Grier et al. 2011; Boroson et al. 2011). Filho et al. (2004) and González-Martín et al. (2009b) fitted the spectra to a MEPL obtaining compatible results with $\log(L(2-10 \text{ keV})) = 39.4$ and $39.2^{+0.2}_{-0.4}$, respectively. Xu et al. (2005) and Grier et al. (2011) by fitting a single PL obtained $\log(L(0.3-10 \text{ keV})) = 39.6$ and $40.0^{+0.01}_{-0.01}$, respectively. Our results ($\log L(2-10 \text{ keV}) = 39.5^{+0.7}_{-0.4}$) are in good agreement with all of them.

In the UV, Cappellari et al. (1999) studied this LINER with both *HST* imaging (FOC) and spectroscopy (FOS), with images taken in 1991, 1993 and 1996 showing long term variability. This is in agreement with Maoz et al. (2005), who used *HST-ACS* observations with its HRC mode and found a 20% variation of the nuclear flux in both F250W and F330W bands.

A.7. NGC 5846

NGC 5846 is a giant elliptical galaxy at the center of a small compact group of galaxies. The inner region of the galaxy contains dust and a radio core (Moellenhoff et al. 1992). Ho et al. (1997) classified this galaxy as an ambiguous case like transient 2.0 object but the revision made by González-Martín et al. (2009b) located this object into the LINERs 2.0 category.

Three *Chandra* observations are archived for this galaxy between 2000 and 2007 and two observations with *XMM-Newton* in January and August 2001. *Chandra* ObsID 788 was analyzed by Filho et al. (2004), Satyapal et al. (2005) and Trinchieri & Goudfrooij (2002). Three different models were fitted (PL, APEC and MEPL), and an order of magnitude difference in luminosity was found between Filho et al. (2004) ($\log L(2-10 \text{ keV}) = 38.4$) and the other two works (39.4 and 39.6 ± 0.4 , respectively), maybe entirely due to the different models used. Our luminosity ($\log(L(2-10 \text{ keV})) = 39.3^{+0.2}_{-0.3}$) is in good agreement with those from Satyapal et al. (2005) and Trinchieri & Goudfrooij (2002). González-Martín et al. (2009b) reported *Chandra* ObsID 4009 from 2003, but we have noticed that obsID 4009 corresponds to the galaxy NGC 5845, not to NGC 5846. The *XMM-Newton* observations reported by

González-Martín et al. (2009b) based in data taken on 2001 were fitted with a ME2PL model resulting in a $\log L(2-10 \text{ keV}) = 40.8_{-2.4}^{+0.0}$, in agreement with our results ($40.2_{\pm 0.0}$).

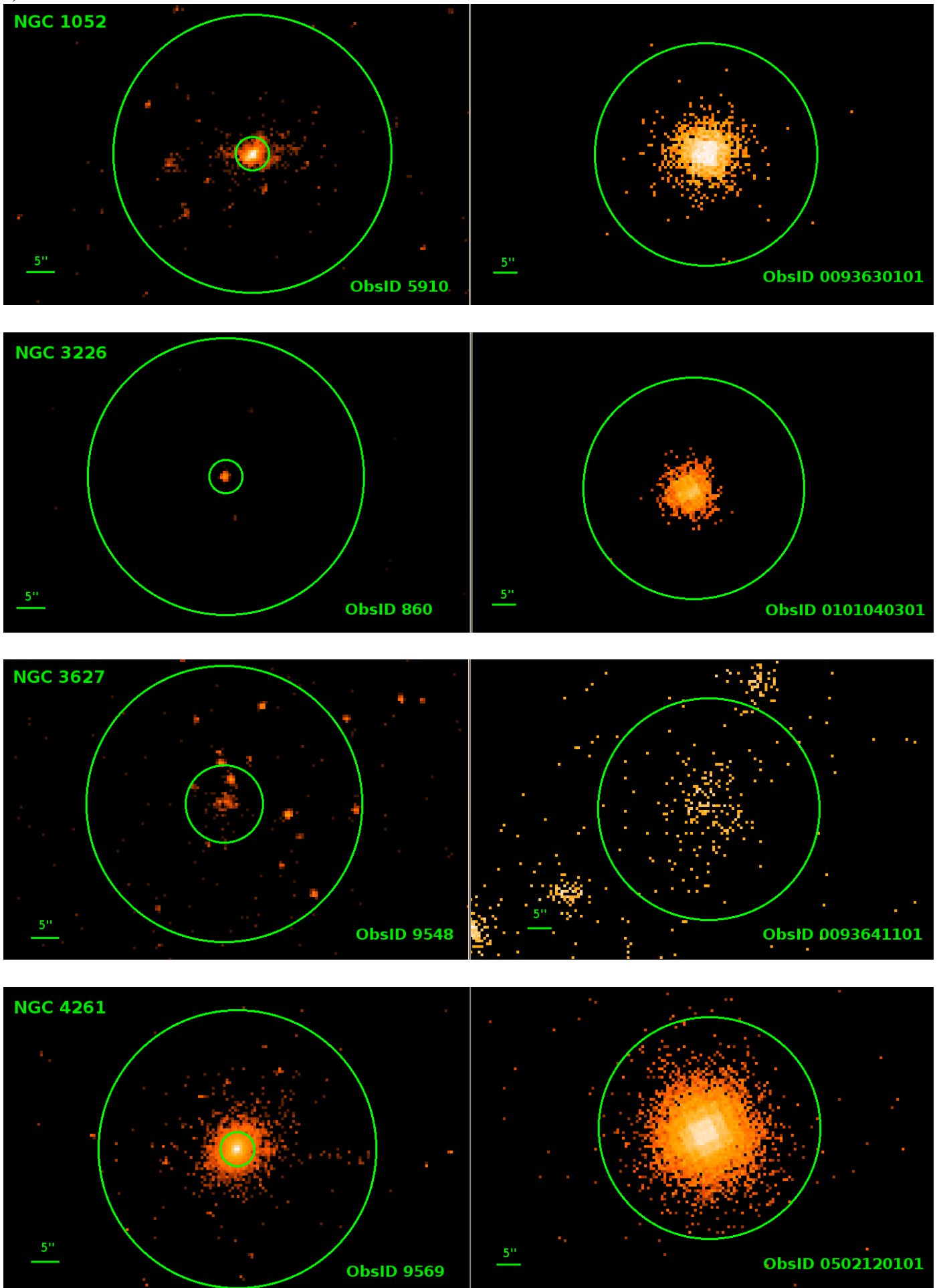
Appendix B: X-ray Images

In this appendix we present the images from *Chandra* (left) and *XMM-Newton* (right) that we used to compare data from these instruments in the 0.5-10 keV band. Big circles represent 25'' apertures. Small circles in the left figures represent the nuclear extraction aperture used with *Chandra* observations (see Table 2). In all cases, the grey levels go from two times the value of the background dispersion, to the maximum value at the center of each galaxy.

Appendix C: Light Curves

The plots corresponding to the light curves are provided.

Fig. B.1. Images for *Chandra* data (left) and *XMM-Newton* data (right) for the sources in the 0.5-10 keV band. Big circles represent 25'' apertures. Small circles in the left figures represent the nuclear extraction aperture used with *Chandra* observations (see table 2).



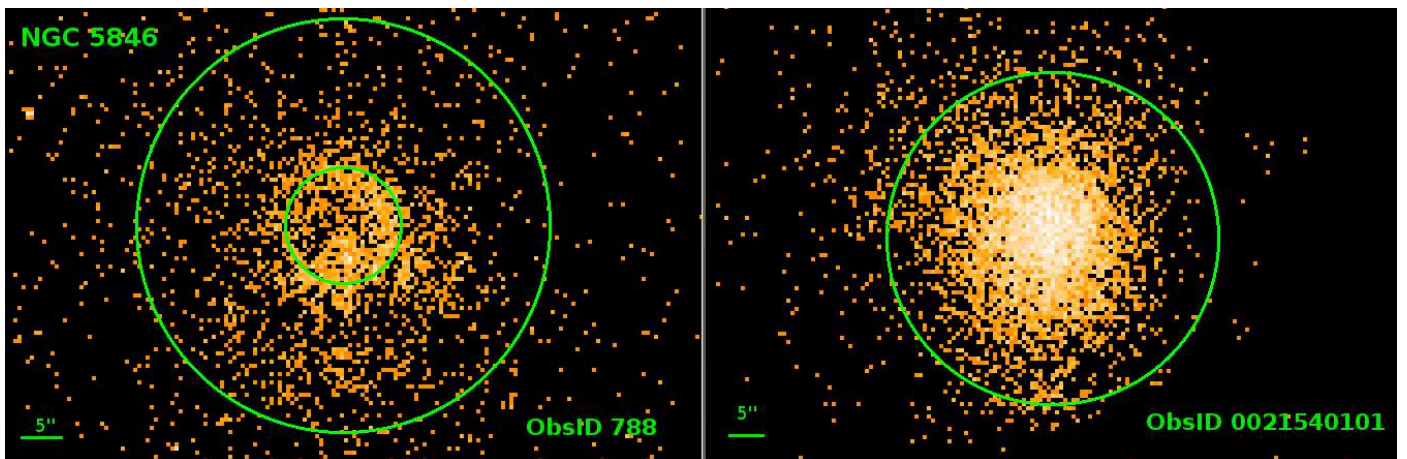
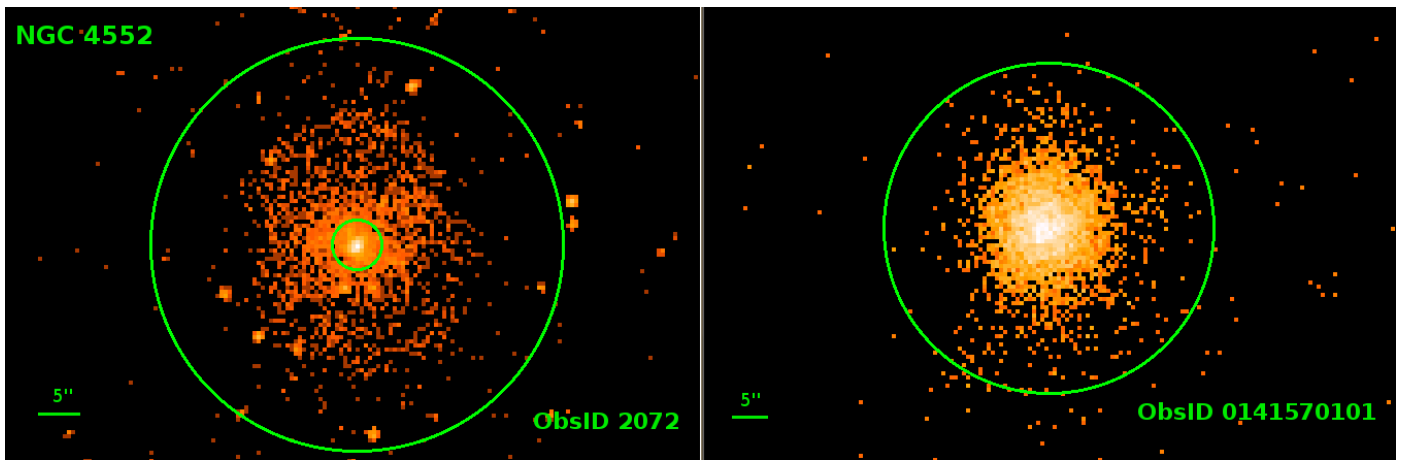
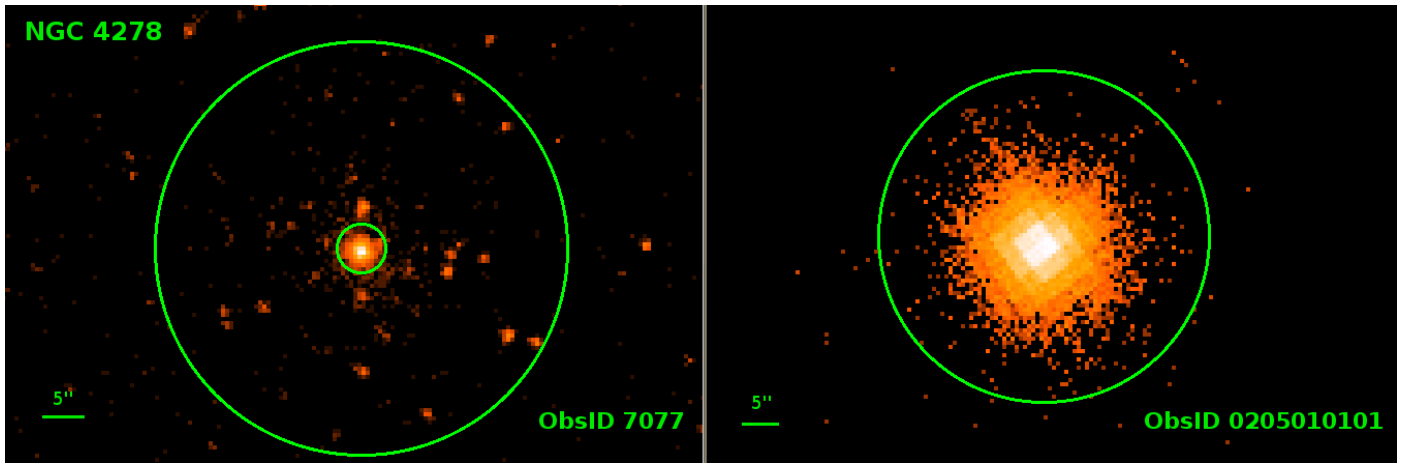


Fig. C.1. Lightcurves for NGC 1052.

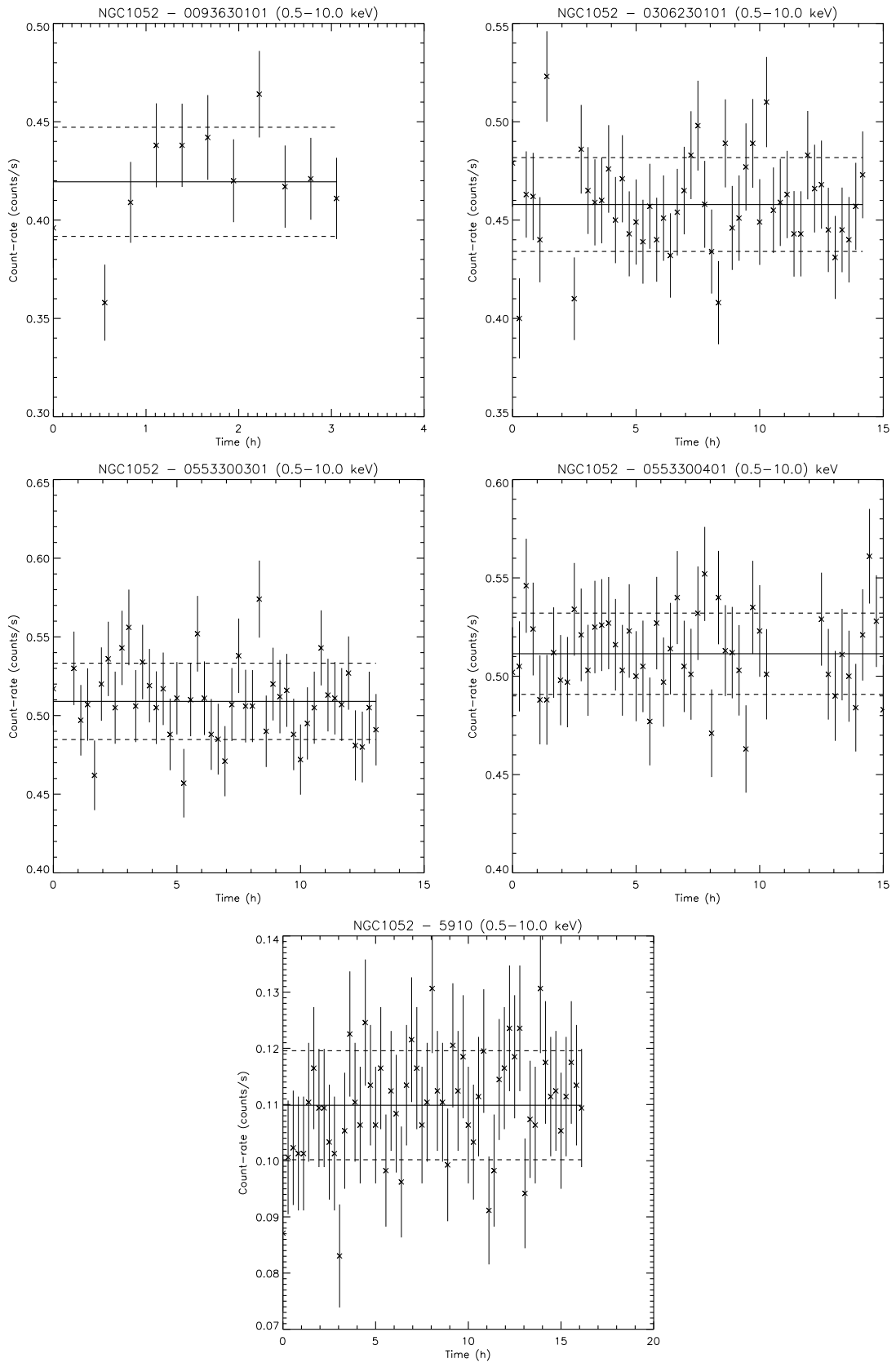


Fig. C.2. Lightcurves for NGC 3226 (up). Light curve from NGC 3227 (middle-right), where the red solid line represents a linear regression, and the light curve from the background (middle-left). *XMM-Newton* obsID 0400270101 image (down). The background follows the same behaviour that NGC 3227.

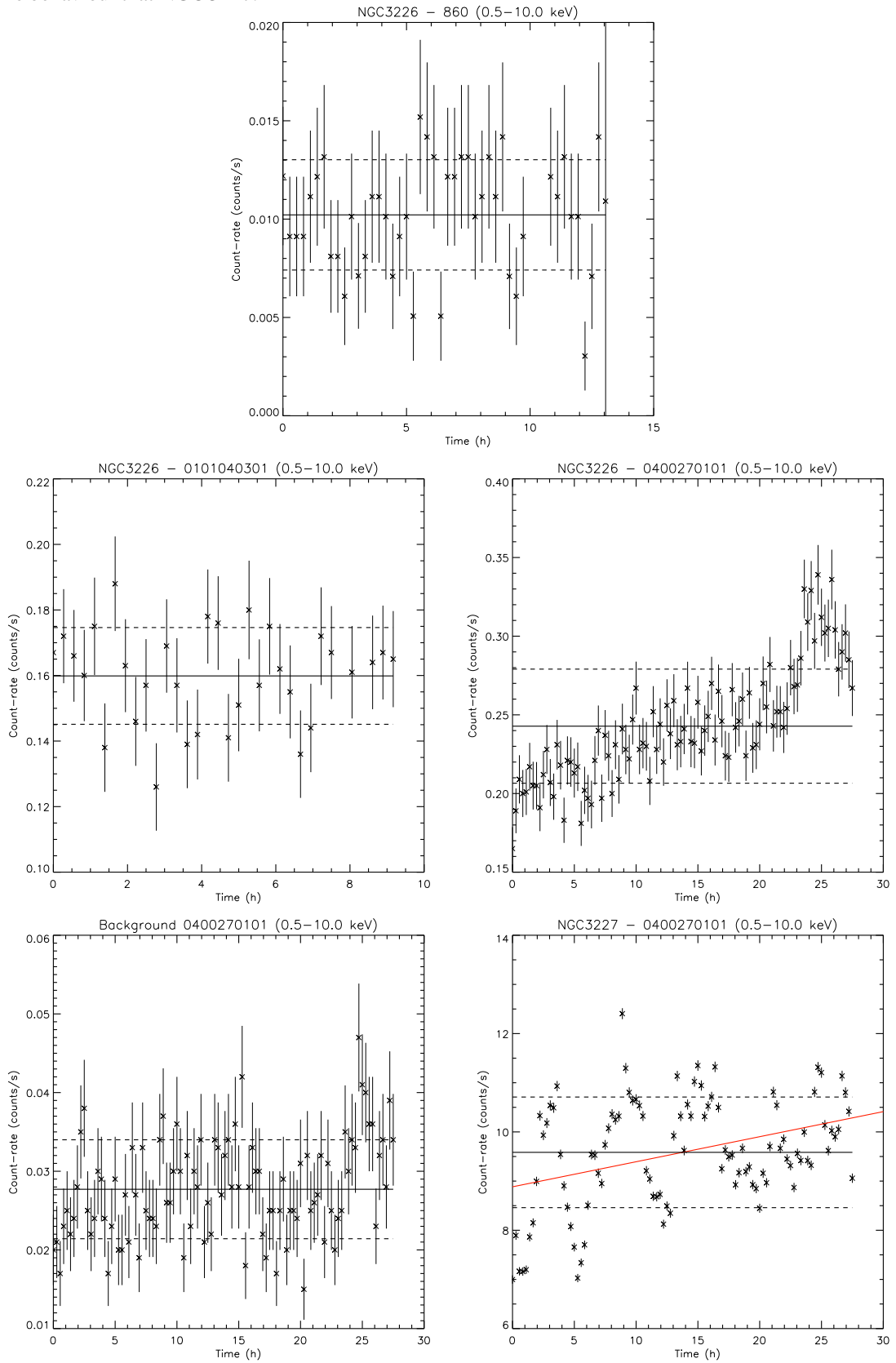


Fig. C.2. Cont.

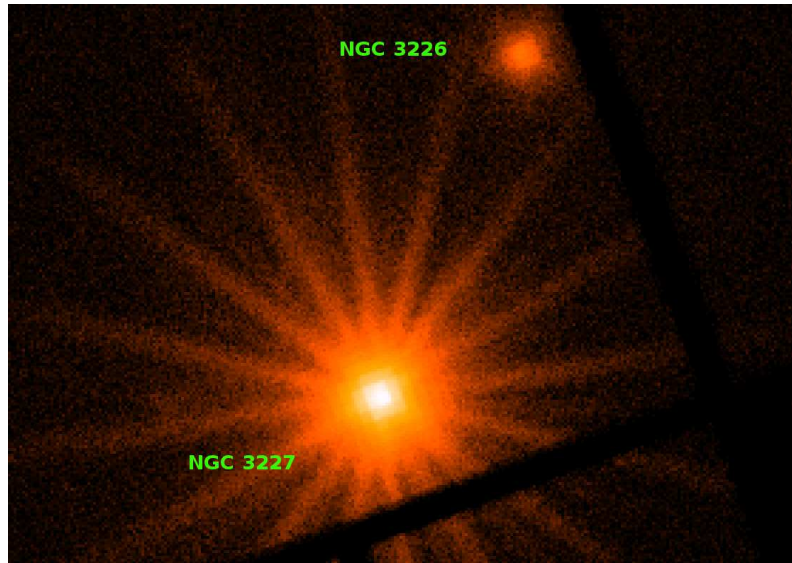


Fig. C.3. Lightcurves for NGC 3627.

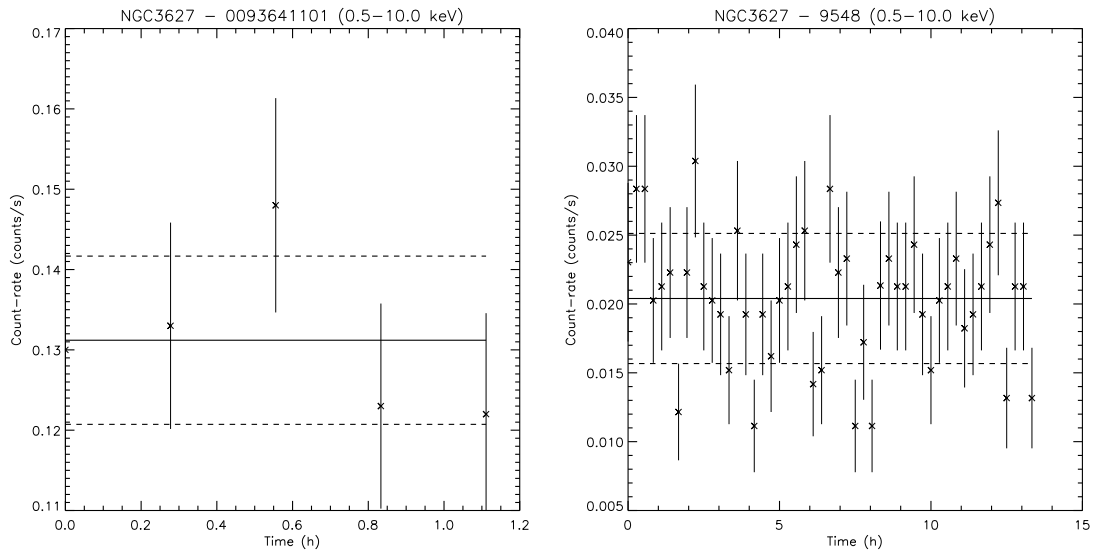


Fig. C.4. Lightcurves for NGC 4261.

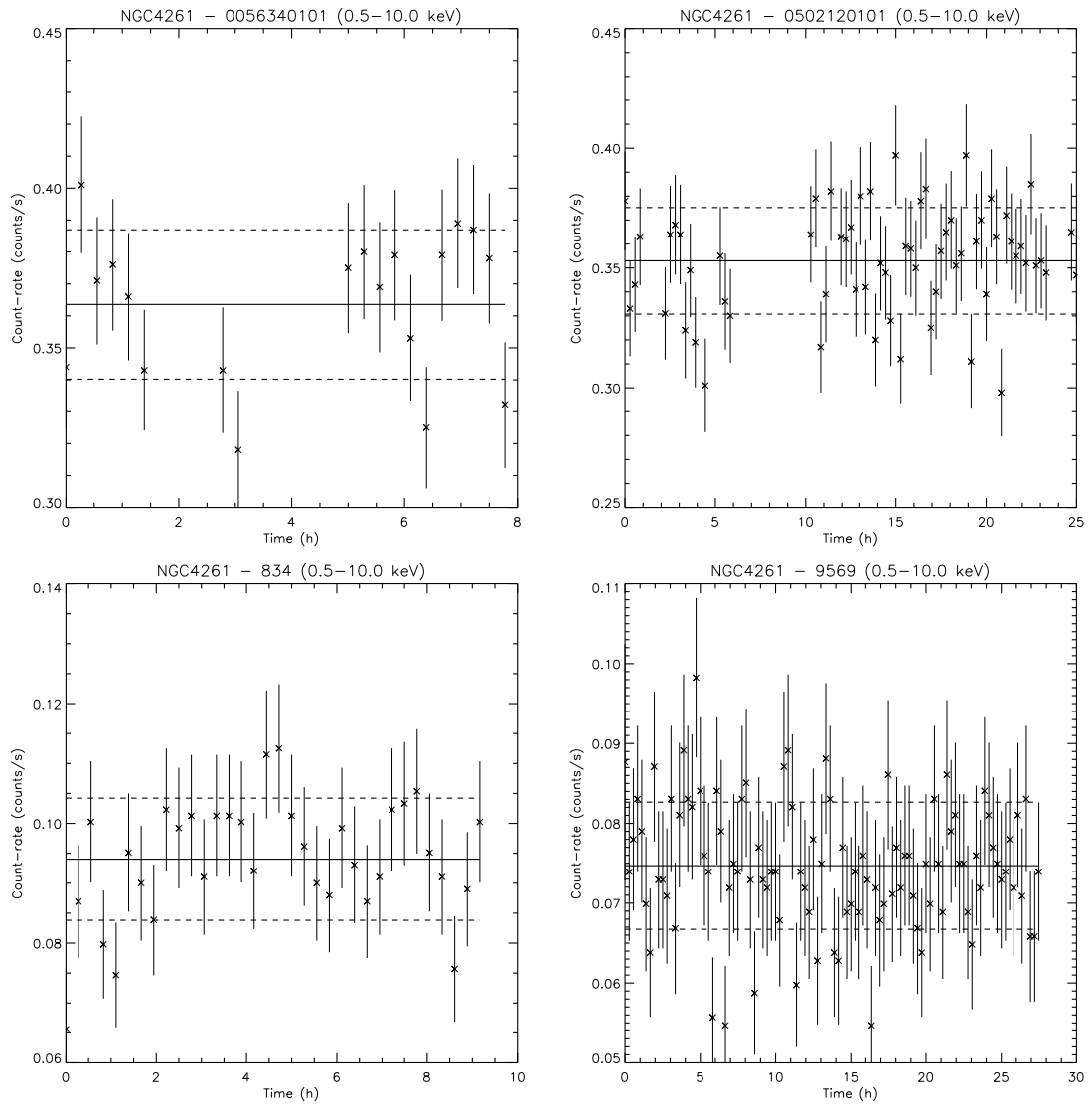


Fig. C.5. Lightcurves for NGC 4278.

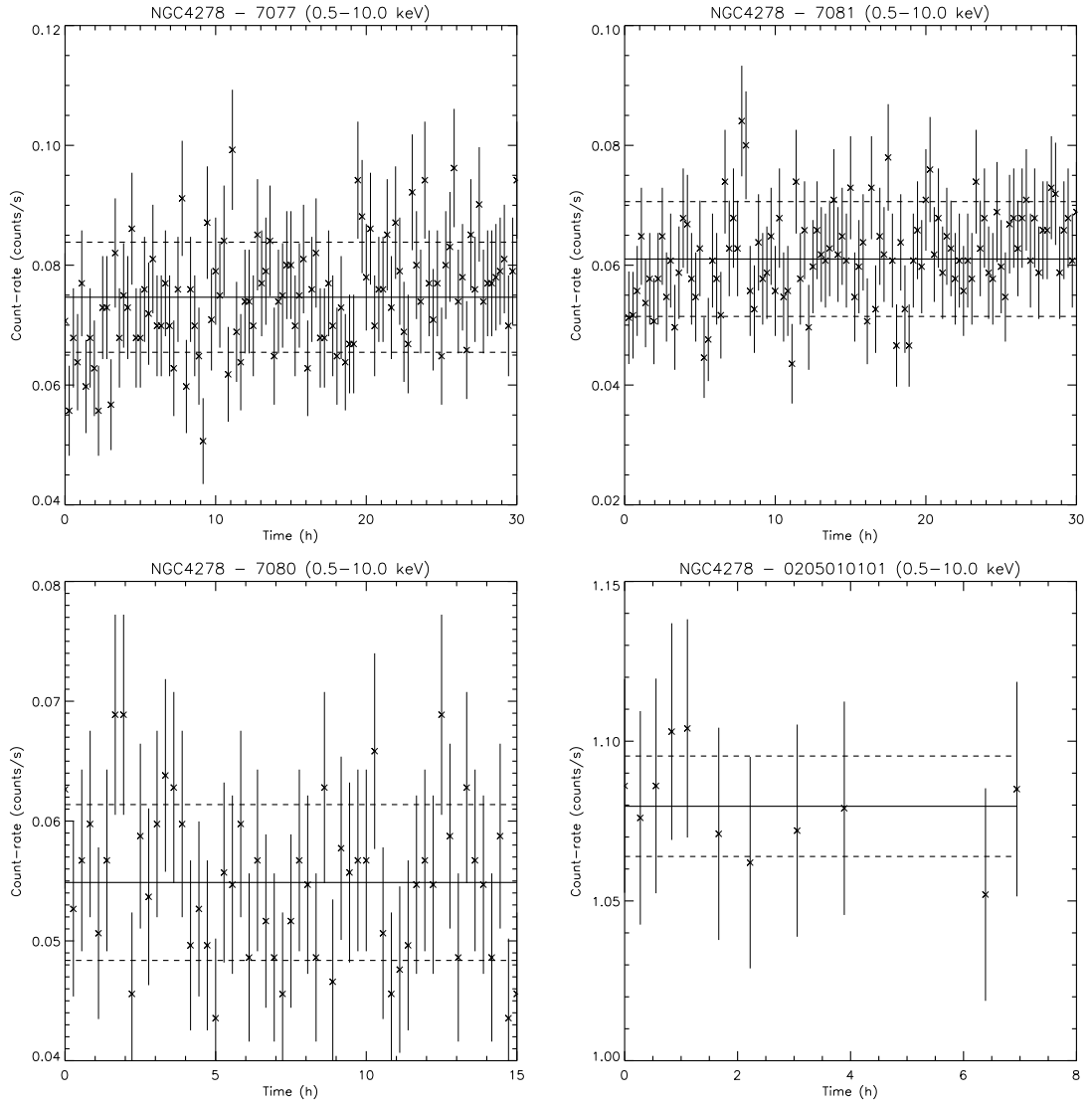


Fig. C.6. Lightcurves for NGC 4552.

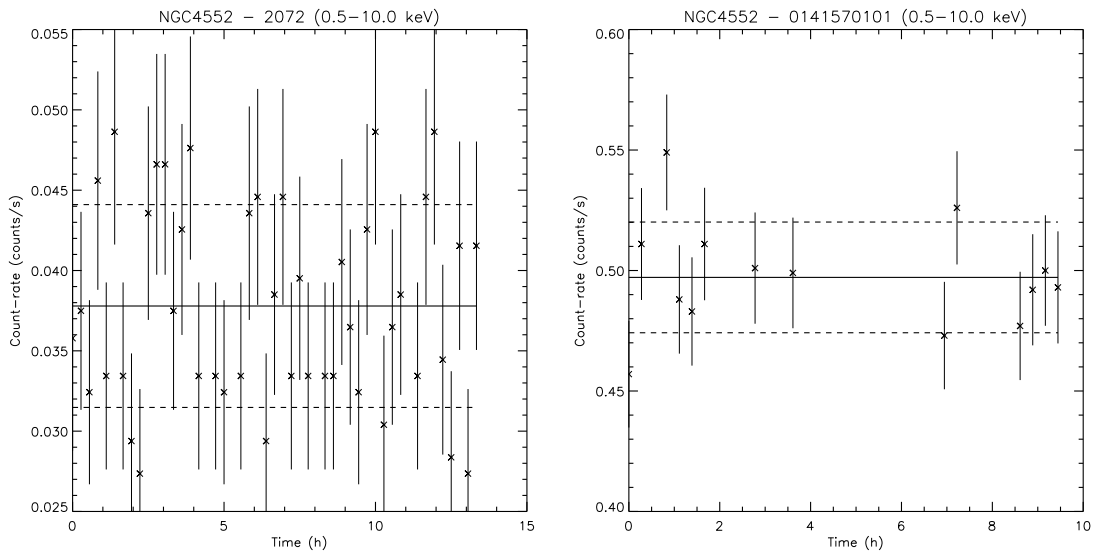


Fig. C.7. Lightcurves for NGC 5846.

